Draft version June 13, 2005
Preprint typeset using LaTeX style emulateapj v. 11/12/01

OBSERVATIONS OF SEPARATOR RECONNECTION TO AN EMERGING ACTIVE REGION

D.W. Longcope, D. E. McKenzie, J. Cirtain and J. Scott
Department of Physics, Montana State University
Bozeman, Montana
Draft version June 13, 2005

ABSTRACT

Extreme ultraviolet (EUV) observations of an emerging active region are used to study separator reconnection in the corona. We identify each EUV loop connecting the emerging polarity to a nearby existing active region over the 41-hour period beginning at emergence onset. Their geometrical resemblance to post-reconnection field lines from a magnetic model of the active region pair implicates separator reconnection in their production. While some reconnection is evident within 7 hours of emergence onset, the most intense period occurs after a one-day delay. The sum of cross sections of all observed loops accounts for only one-fifth of the transferred magnetic flux predicted by the model. We suggest that the remaining loops remain at temperatures too high, or at densities too low, to be detected in our EUV data. The most intense reconnection requires as much as 10^9 Volts along the coronal separator, however, the observed loops suggests that the flux is transfered as discrete bundles of $\sim 4 \times 10^{18}$ Mx each. The reconnection appears to directly dissipate only a small fraction of the energy released, while the rest is dissipated within the post-reconnection flux over the ensuing 6 or more hours the loops remain visible. The net energy released, and ultimately dissipated, is consistent with the amount which could be stored magnetically during the 24-hour delay between emergence and reconnection.

1. INTRODUCTION

Magnetic reconnection has been proposed to explain a wide variety of coronal activity including flares (Sweet 1958), coronal mass ejections (Antiochos 1998), coronal bright points (Golub et al. 1977) and ubiquitous coronal heating (Parker 1972). Of these, solar flares are the most often studied manifestation of reconnection. Many aspects typically observed in eruptive flares, such as separating flare ribbons, X-ray cusps and post-eruption down-flows, have been attributed to consequences of reconnection in the scenario of Carmichael, Sturrock, Hirayama, Kopp and Pneumann (CSHKP, see McKenzie 2002, for a review).

Due to their complex geometries, however, flares are poor contexts in which to study reconnection in detail. Reconnection is assumed to be responsible for the rapid energy release and possibly for energy dissipation, so the reconnection rate is presumed to be reflected in the intensity of flare emission. It has proven extremely difficult, however, to actually measure the *rate* of reconnection, defined as the rate at which field lines are topologically changed. The only studies which could qualify as such measurements have tracked the motions of chromospheric features, such as hard X-ray footpoints or flare ribbons (Fletcher & Hudson 2001). Since these signatures are considered to be magnetically linked to the reconnection site it is argued, usually from the two-dimensional CSHKP picture, that the speed of apparent motion is related to the rate of reconnection.

Coronal loops connecting between two active regions offer some of the most compelling evidence of non-flaring reconnection in the solar corona (Sheeley et al. 1975; Tsuneta 1996; Pevtsov 2000). An active region is generally assumed to be produced by the buoyant emergence of one or more flux tubes from below the photosphere (see Fisher et al. 2000, and references therein for a review). Under this assumption, any coronal field interconnecting two distinct regions must have been produced through magnetic reconnection after emergence. The conclusion is particularly compelling when the loops interconnect active regions from opposite hemispheres.

In his pioneering study of reconnection between active regions Tsuneta (1996) analyzed *Yohkoh* Soft X-ray telescope (SXT, Tsuneta et al. 1991) images of the bipolar active regions 7116 and 7117 which interacted across the equator between 23 March and 2 April 1992. Many of the SXT images show four distinct loop sets arranged in a symmetric X, resembling a magnetic X-point. Detailed analysis revealed that the interconnecting loop sets (East and West of the X) , which had been presumably formed by reconnection at the X-point, were 2–3 times hotter than the loops internal to the active regions (4–7 MK *vs.* 2 MK). Tsuneta found that the post-reconnection flux would be heated sufficiently if all the energy of a 18–27 G upstream magnetic field were dissipated (converted to heat) as it passed the X-point at one percent of the upstream Alfvén speed. This reconnection seems to have progressed steadily, without explosive manifestations such as flares, and the magnetic structure of each active region changed continuously in accordance.

Tsuneta's study remains a valuable contribution to our present understanding of reconnection in the corona. The theoretical interpretation it proposes, Petschek reconnection at a magnetic neutral point, does present persistent difficulties. It is remarkable how clearly the SXT images, especially in the period around 27 March 1992, resemble the classic right-angle separatrices of a two-dimensional X-point. This is exactly the configuration we would expect if the magnetic field were current-free. Such a current-free field, however, would have no free energy to dissipate through reconnection. Furthermore, the brightest interconnecting loops are often very far from the X-point where they were supposedly energized. This separation is particularly puzzling in light of the rather short time,

~ 450 sec, in which the author estimates the loops should conductively cool. Finally, it is not possible for a significant quantity of magnetic flux to pass through an isolated neutral point, or even through a neighborhood of that point. Three-dimensional reconnection models predict instead that reconnection must occur along a magnetic separator (Greene 1988; Lau & Finn 1990). The rate of reconnection will be given by the voltage difference between the two ends of the separator field line (Sweet 1958; Longcope 1996).

The basic approach of studying non-explosive reconnection between active regions, which Tsuneta (1996) pioneered, remains among the most promising avenues for quantifying reconnection and thereby illuminating its basic physical underpinnings. In this work we analyze data from the period 2001 Aug. 10–11, during which active region 9574 emerged in the immediate vicinity of existing active region 9570. The emergence occurred as the pair crossed disk center and as the Transition Region and Coronal Explorer (TRACE, Handy et al. 1999) was making high-cadence observations of that area in the 171 Å passband.

The TRACE observations show numerous loops interconnecting the two regions and thereby provide an unprecedented opportunity to quantify magnetic reconnection. We herein use these observations to measure the reconnection rate, defined as the rate magnetic flux is topologically changed. We find that the reconnection rate is relatively small for the first ~ 24 hours of emergence and then rapidly increases to a peak as high as 10^{17} Mx/sec (10^9 Volts). Comparison to a three-dimensional magnetic model reveals the interconnecting loops are consistent with those produced by reconnection at a separator overlying the volume between the active regions. In this model the reconnection rate is the electromotive force (EMF) along the separator.

While the observations provide evidence that the interconnecting loops were formed by separator reconnection, they also suggest that the reconnection *did not* heat the loops significantly, at least not at the instant of reconnection. The pre-reconnection free magnetic energy predicted by the model is sufficient to provide all the heat ultimately observed. The long duration of the TRACE loops, in excess of their radiative cooling times, and their delayed appearance relative to soft X-ray loops observed by *Yohkoh* SXT, suggest that the heat was instead deposited over many hours following the moment of reconnection.

The present work presents the data, the measurements and theoretical interpretation as separator reconnection in the following order. The next section presents the TRACE data set and describes the construction of a stack plot from it. Section 3 describes the magnetic data and its use in the production of a three-dimensional coronal model. Section 4 uses the stack plot and magnetic model to calculate the reconnection EMF. The magnetic model also predicts the free energy stored in the coronal field during the 24-hour delay between emergence and reconnection. Section 5 discusses the quantitative and qualitative implications of these observations. The last section presents a very brief synopsis of the observations and organizes them in terms of the magnetic model.

2. CORONAL OBSERVATIONS

The principal coronal data consist of 768×768 pixel 171Å TRACE images made between 2001-Aug-10 7:00 and 2001-Aug-11 23:59, of the emerging active region 9574 and its neighbor AR9570. (We chose not to use the 1600 Å, white light, or 1024×1024 171 Å images which were made by TRACE at much lower cadence over this same period.) During this 41-hour interval 5,139 images (768×768 pixels) were obtained, at an average cadence of one every 28 seconds (see fig. 1). These were processed using standard software for flat-field correction, removal of cosmic ray "spikes" and division by exposure time. After this, a uniform coronal background was subtracted (see Cirtain 2005, for details). Figure 1 is an example, from 11:00 Aug-11, showing a portion of AR 9574 along the top, all of AR 9570 and several interconnecting loops.

In order to identify each and every interconnecting loop we define a horizontal line separating AR 9570 from AR 9574. The line is located $195.7''$ South of disk center at 11:00 Aug-10 and is occasionally repositioned to accommodate the expansion of AR 9574. The line is shifted northward several times as AR9574 is first emerging and then southward in steps of 5" or 10" as needed. After the final shift, at 04:00 on Aug-11, the line is located at $y = -215.7''$.

A synthetic slit consisting of a 600×3 strip of pixels lying along this line, is extracted from each processed image (see fig. 1). The slit is repositioned horizontally every hour or two to compensate crudely for solar rotation. The result, after averaging over the 3-pixel height of the strip, is a 600×5139 array of 171Å intensity values. A final stack plot is then produced by averaging the slit-images into even-time bins of $\Delta t = 3$ minutes. To compensate more precisely for solar rotation, the left pixel of each time-bin is rotated to its position at 11:00 Aug-10. Figure 2 shows the resulting stack plot, along with the loops and elements of the magnetic model described below.

Each pixel of the stack plot results from two different averages. First there is a spatial average across the 3-pixel-high slit, and then a temporal average over 3 minutes. As a result the data in the stack plot has lower noise than the raw data. A histogram of pixels from a very dark section of fig. 2 has a width of $\sigma = 0.17$ DN/sec. We take this as the noise level over the entire stack plot.

Interconnecting loops appear as slanted dark streaks in the stack plot (fig. 2). Within a single intensity time slice, $I(x)$, a loop appears as a peak located where the loop crosses the slit. Intensity peaks are identified automatically by an algorithm which first locates local maxima in a smoothed curve, $\mathcal{S}I(x)$. The peak unsmoothed intensity must exceed 0.75 DN/sec. Neighboring pixels are then assigned to that loop provided they are strictly downhill in the smoothed intensity $\mathcal{S}I(x)$ and also have an unsmoothed intensity, $I(x)$ above one half the peak's value. The downward extent from the peak must exceed 0.75 DN/sec in at least one direction in order for the loop to be deemed distinct from its neighbors. Figure 3 shows the smoothed and unsmoothed curves, $\mathcal{S}I(x)$ and $I(x)$, at 5 different times. Peaks identified by the algorithm are denoted by asterisks and the extent of the loop by a horizontal bar. These examples show several instances, such as one at the right of the top curve ($x \simeq -165$ for $t = 36.47$)

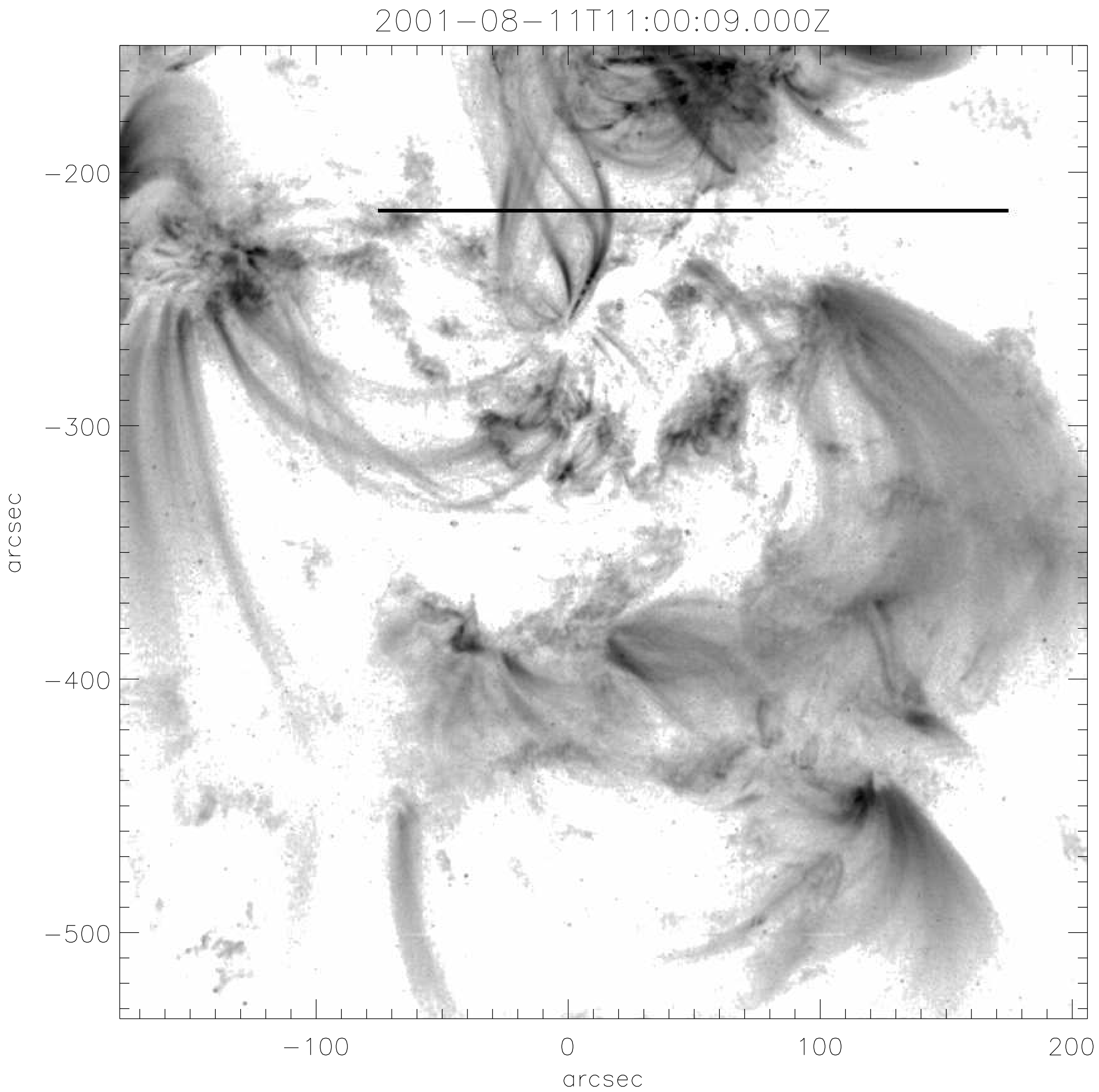

FIG. 1.— TRACE 171Å image of AR 9570 and AR 9574 from 11:00 Aug-11, plotted as an inverse grey-scale of the square-root of the background-subtracted count rate. Axes are in arc-seconds from disk center. The emerging active region, AR 9574, is partially cropped by the top of image; the older active region is located around $y = -250$. The 600×3 pixel horizontal strip, centered at $y = -214.7''$, is shown as a dark horizontal line.

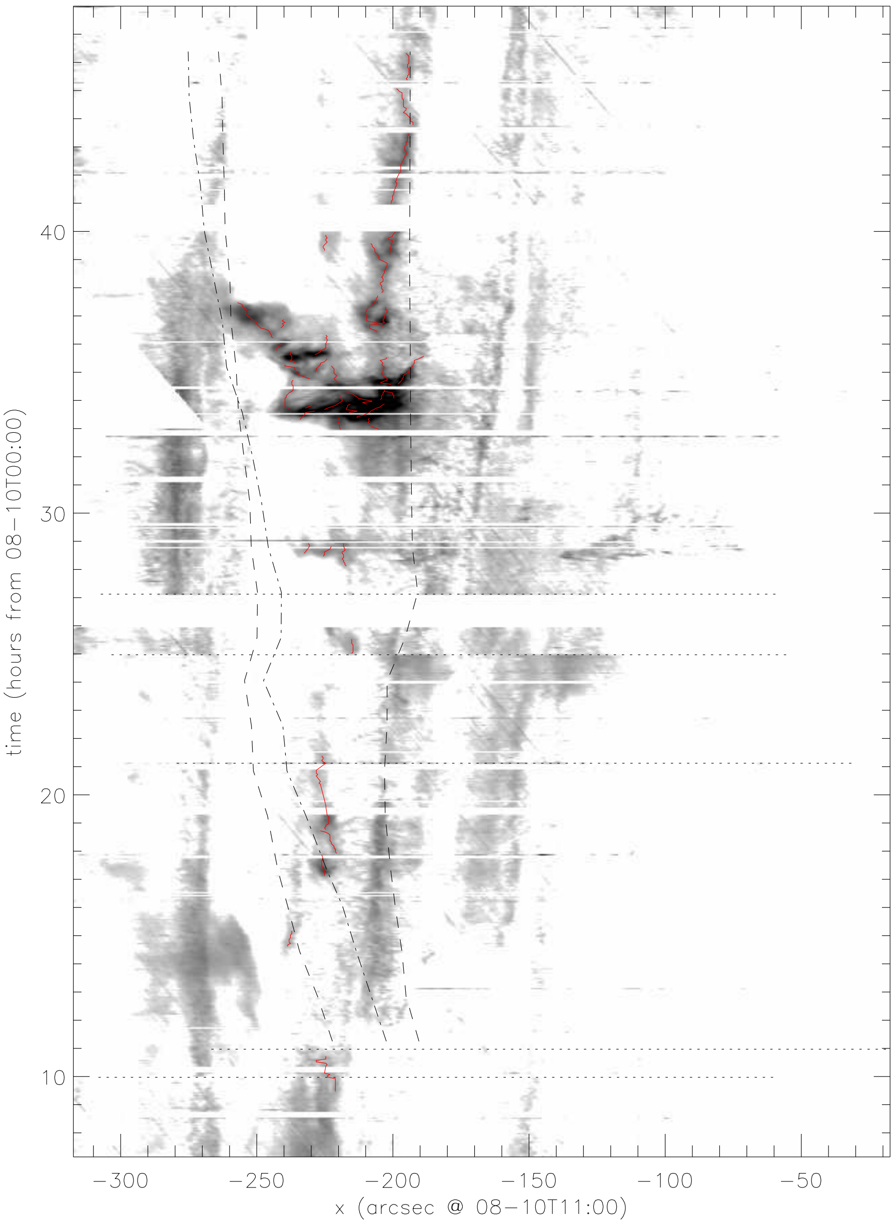

FIG. 2.— The stack plot from TRACE 171Å within the horizontal slit. Inverse grey-scale shows data numbers (DN) per second within the 3-pixel high strip between the active regions. The horizontal axis is the spatial coordinate, in arc-seconds from disk center, rotated back to 11:00 Aug-10. The vertical coordinate is time in hours since 00:00 Aug-10. Dashed and dash-dotted lines are separatrices and separators from the magnetic model. Red solid curves indicate each of the loops identified in the stack plot and the images. The horizontal dotted lines denote the times at which the slit was moved vertically to accommodate the expansion of AR 9574.

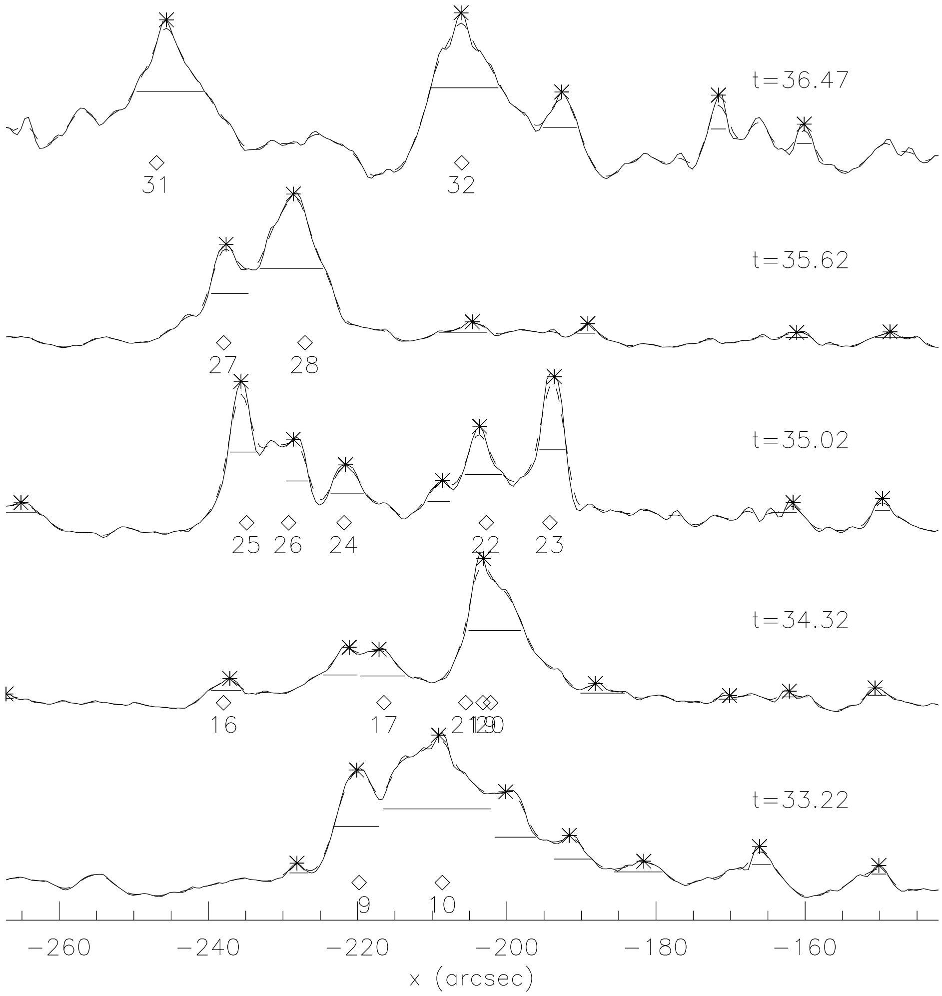

FIG. 3.— Five time-slices from the stack plot fig. 2 from $t = 33.2$, 34.3, 35.0, 35.6 and 36.45 hours after 00:00 Aug-10 (i.e. from 9:12, 10:17, 11:00, 11:54 and 12:27 on Aug-11). Solid and dashed curves show the unsmoothed and smoothed intensities $I(x)$ and $\mathcal{S}I(x)$ respectively. Each curve is normalized to the global maximum of $I(x)$ for that time. Local maxima of $\mathcal{S}I$ are denoted by asterisks, and the the pixels associated with that peak are indicated by a horizontal bar at the half-max level. Numbered diamonds are the peaks associated with legitimate coronal loops.

where the peak has been deemed indistinguishable from neighboring peaks by the required 0.75 DN/sec.

When the automatically-identified peak locations are vertically stacked, as in fig. 4, genuine loops stand out in tilted rows while spurious peaks appear as isolated dots. Each row of three more more points falling on a roughly straight line was manually selected from such a plot and designated as a loop. A continuous row of points with an abrupt direction change (i.e. change in apparent velocity) was considered to be two distinct loops, such as loops 36 and 37 in fig. 4. After all rows of points were selected, their locations were then over-plotted on a spatial image as shown in fig. 5. Identifications which appear to be something other than a loop or which appeared to be a non-interconnecting loops crossing the slit, were eliminated from the loop list. There are several instances where a row of vertical (stationary) points correspond to generalized low-altitude brightenings such as "moss" (Berger et al. 1999).

The final result of this procedure was a complete list of 43 interconnecting loops that we number 0–42 in order of appearance. The very fist loop, Loop 0 at 9:27 Aug-10, is the earliest hint in 171Å of a connection between active regions. Prior to this the leading pole of AR9570 has numerous radial loops fanning out like spokes, producing the enhancement at $x \simeq -230$ of the stack plot (fig. 2). At 9:27 one spoke appears to be aimed toward the emerging AR, and we take this as the first interconnection, Loop 0, even though its northern footpoint is invisible. The second loop, Loop 1, appears at 14:36 and is unambiguously an interconnecting loop. All subsequent loops, such as Loop 2 shown in fig. 5, have the same unmistakable interconnecting form.

Each of the 43 loops is characterized by parameters found from the stack plot. Loop 1, for example, remains bright in 171Å for 36 minutes, in the sense that its peak is identifiable as described above. Its diameter is 1.8 Mm, found from the median over all times of the full width at half maximum at each time. The crossing point moves westward at an average speed of 543 m/sec, resulting in a right-tending streak on the stack plot (fig. 2). The streak is 1.12 DN/sec in its brightest pixel, but has a mean intensity of $I = 0.79$ DN/sec over its 36 minute duration.

Loop 1 turns out to be among the faintest of the entire set, perhaps because it is the first genuine interconnection. Although its peak intensity is small (1.12 DN/sec) it is well above the noise floor which we earlier estimated to be $\sigma = 0.17$ DN/sec. Subsequent loops have peaks in the range 1.5–5 DN/sec, until loops 10–23, starting at 8:57 on Aug-11, which have peak emissions in the range 10–40 DN/sec. Thereafter loop peak intensities return back to a level 1–10 DN/sec. We return below to discuss the significance of the period of brighter interconnecting loops.

The intensity I of a loop puts a lower bound on its electron density. The response of the TRACE 171Å imager reaches a maximum, $R_{\rm max} = 1.1 \times 10^{-26}\,{\rm DN\,s^{-1}\,cm^5}$ in a single pixel, at a temperature of $T_e = 0.95 \times 10^6$ K (Aschwanden et al. 2000). Assuming the loop to be uniformly filled across its diameter, d, with plasma at the optimal temperature provides a lower bound on the electron density of the loop

$$n_e = \sqrt{\frac{I}{R_{\rm max} d}} \quad . \tag{1}$$

The density bound for Loop 1 is $n_e = 6.3 \times 10^8\,{\rm cm^{-3}}$ using its mean intensity, but is no less than $n_e = 7.5 \times 10^8\,{\rm cm^{-3}}$ at the instant of peak emission.

The values found for all 43 loops are summarized in the histograms in fig. 6. From these it appears that loops are typically $\sim$ 3.7 Mm (the median of all medians), which move across the slit at around 1 km/sec. The density histogram in fig. 6 shows the lower bound from the mean intensity value of each loop, as defined by eq. (1). The majority of loops have values of 0.5–$1.0 \times 10^9\,{\rm cm^{-3}}$ for this lower bound. For 4 Mm diameter loops, typical of the ones observed, the detection threshold of 0.75 DN/sec corresponds to an average electron density of $n_e = 0.4 \times 10^9\,{\rm cm^{-3}}$; this is taken as the detection limit in our analysis.

Of the total background-subtracted EUV intensity along the slit, most comes from the interconnecting loops we have identified. The dashed lines in stack plot fig. 2 are from a magnetic model explained below. It is evident that they encompass, for the most part, that segment of the slit where interconnecting loops occur. Integrating the emission across this segment and out to 20" beyond it, gives the dashed line in fig. 7, which we consider the total EUV emission. The solid curve is the corresponding emission from only those pixels in the identified loops. This can be seen to be a significant fraction of the total. In some cases the total intensity is actually *less* than that part in identified loops. This occurs due to negative contributions from the surrounding regions, resulting from background subtraction. Although at most times the loop-attributed intensity is the majority of the total intensity, obvious exceptions occur at $t = 25$ and $t = 32$. These are found, by examination of the stack plot fig. 2 and corresponding spatial images, to result from general brightenings of diffuse emission such as moss. This appears in the $t = 33.0$ time-slice, the bottom curve in fig. 3, as broad emission between $x = (-210, -190)$.

3. THE MAGNETIC MODEL

3.1. *The magnetic data*

Magnetic data of the active region's emergence is provided by full-disk magnetograms made every 96 minutes by the SOHO/MDI instrument (Scherrer et al. 1995). A subregion was extracted from each full-disk magnetogram and the measured values were multiplied by the calibration factor 1.56 following Berger & Lites (2003). Polarity concentrations were automatically identified by locating local maxima in a smoothed magnetogram and associating with each maximum all surrounding pixels which are both downhill in the smoothed magnetogram and which have values of $B_{\rm los}$ above 45 G. Regions with fewer than 40 pixels were then discarded. Examples of the raw magnetograms and identified concentrations are shown in fig. 8.

A magnetic model of the active region complex was constructed from the identified polarity concentrations. The flux of each concentration is found by summing the pixels from line-of-sight measurement and increasing them by a

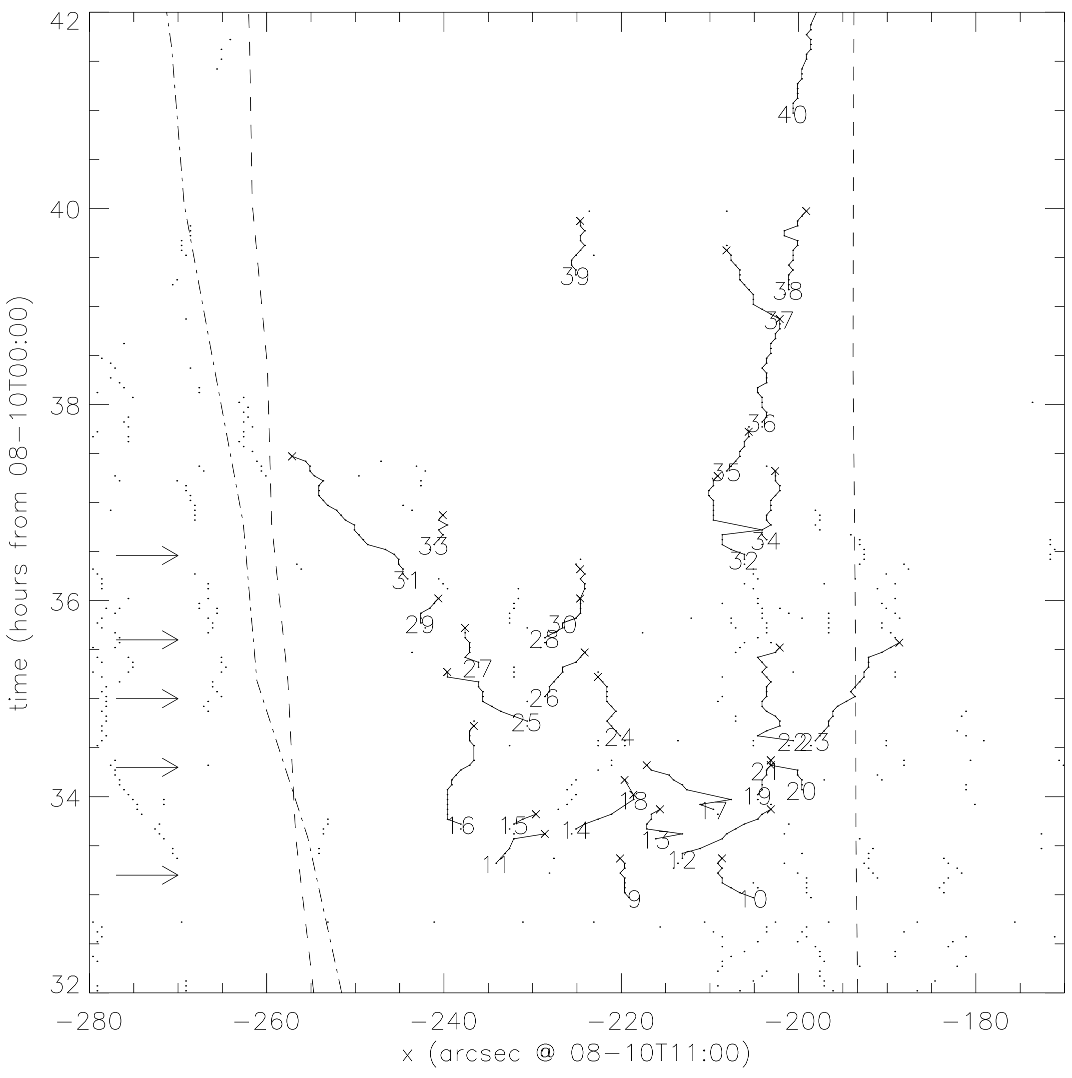

FIG. 4.— Peaks and loops from the stack plot. Dots indicate the peaks identified from maxima in time slices. Numbered curves are loops. Five arrows along the left indicate the times of the profiles shown in fig. 3 and to panels 4–7 of fig. 5.

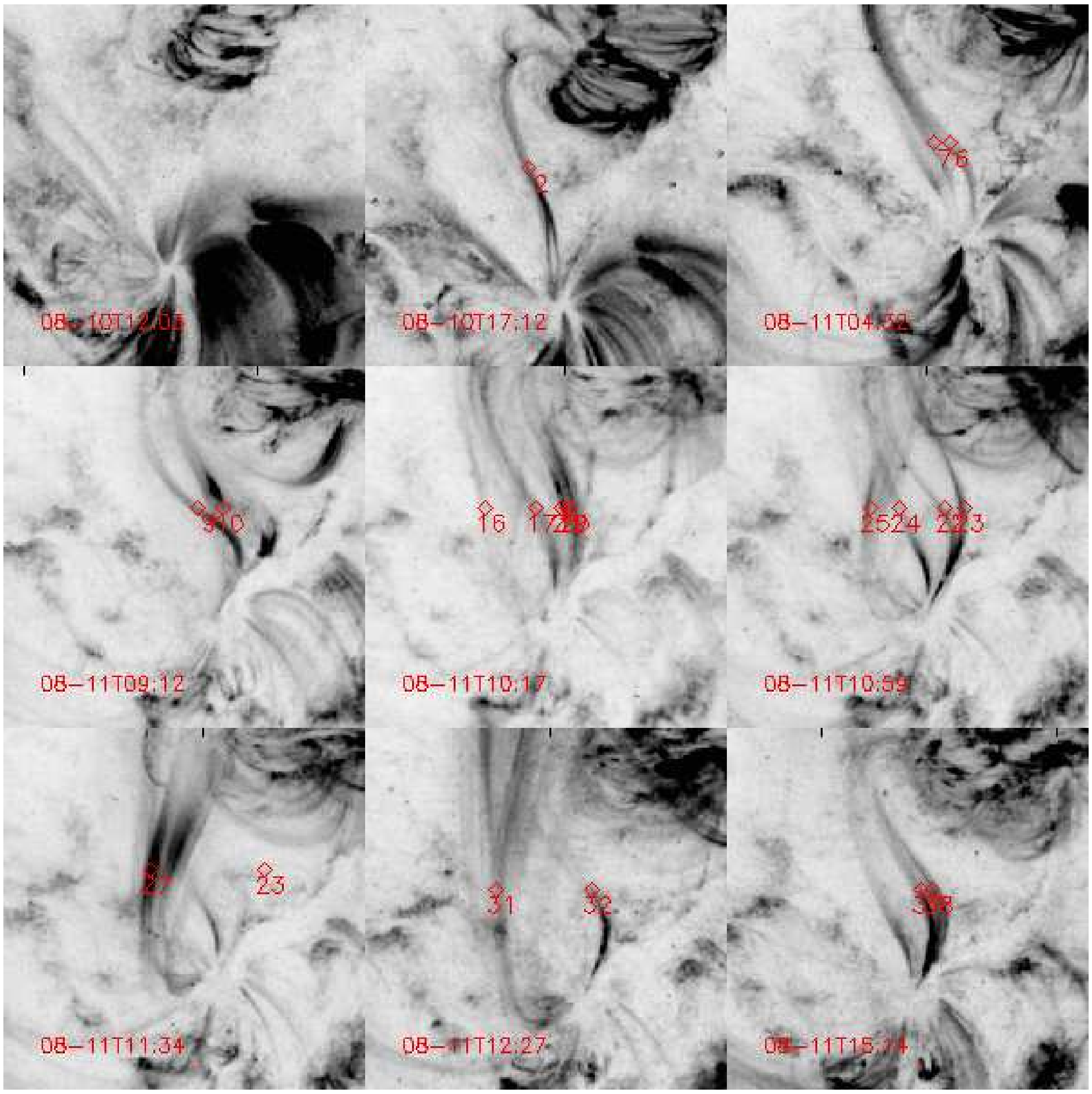

FIG. 5.— A composite of interconnecting loops from the emergence of AR9574. Nine selected times read chronologically from left to right, top to bottom; times are indicated in the lower left of each image. Diamonds are the identified loops. Panels 4–7 correspond to profiles in fig.3.

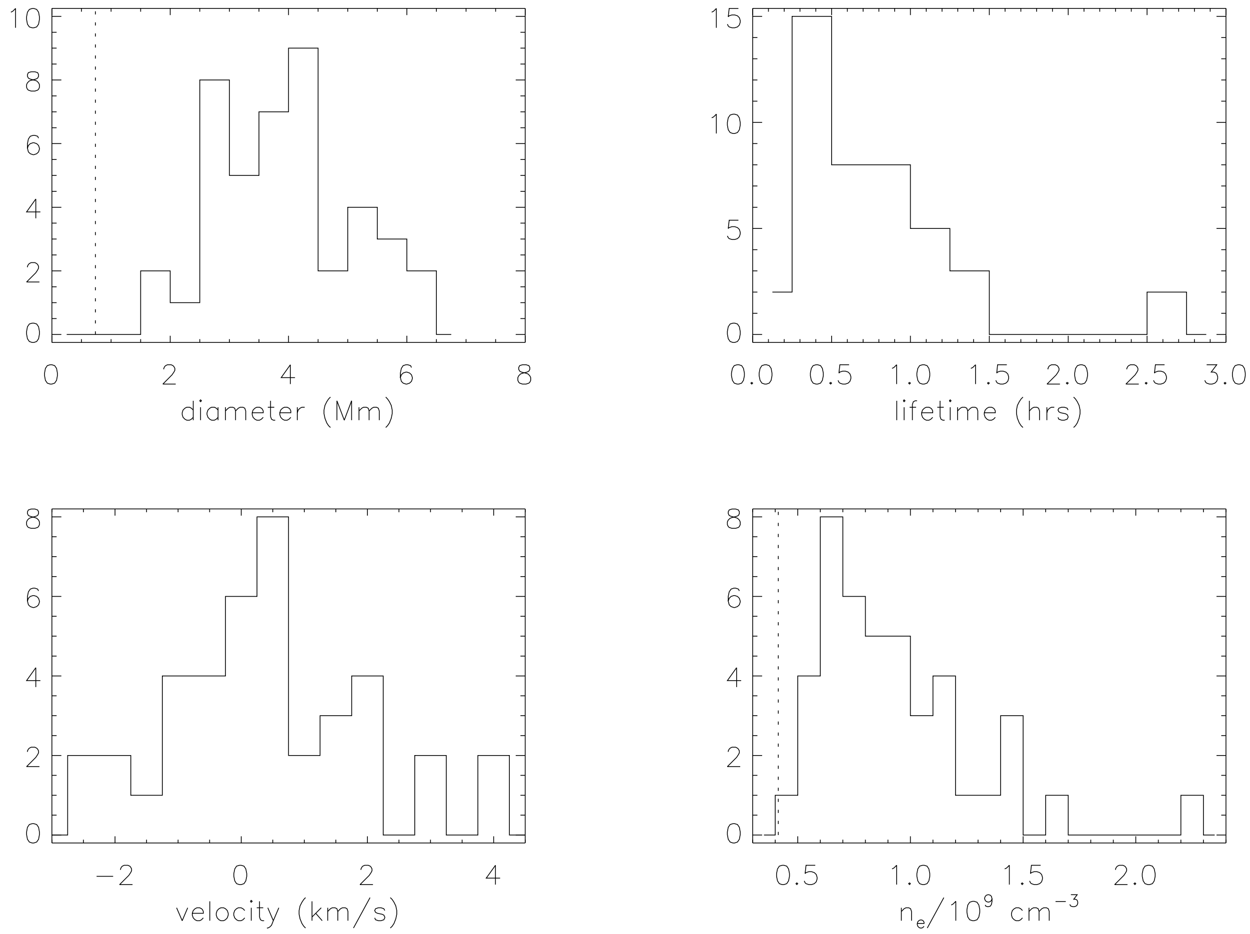

FIG. 6.— Histograms summarizing properties of the 43 loops interconnecting AR 9570 and 9574. A vertical dotted line marks the Nyquist limit, two-pixels, on the diameter plot. The vertical dotted line on the density histogram is the density of a loop at the detection threshold of 0.75 DN/sec whose diameter is the typical value of 4 Mm.

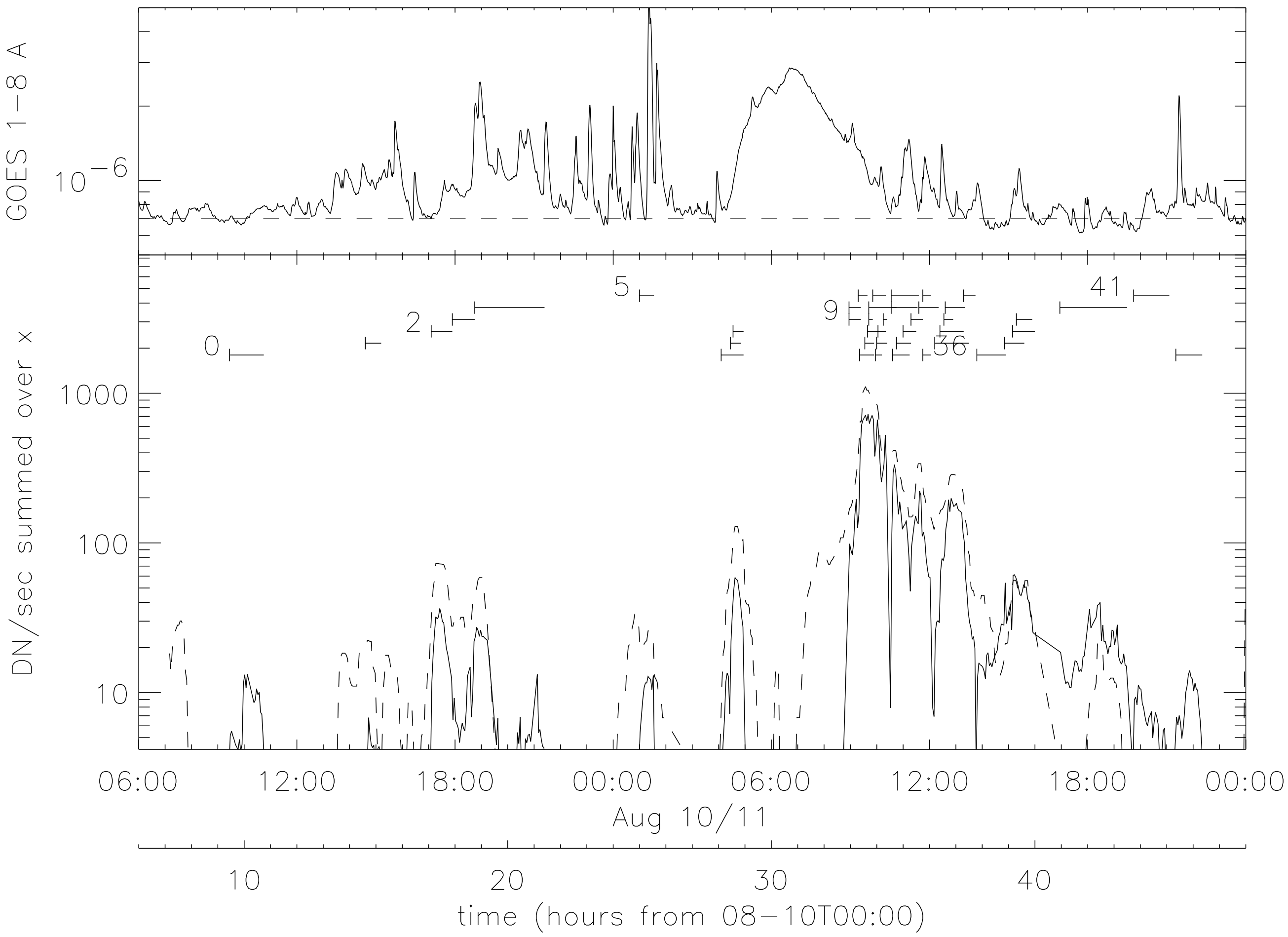

Fig. 7.— Time histories of the emissions from reconnected flux. The lower panel shows the integrated 171 Å emission from loops (solid curve) and from all pixels within the interconnecting region (dashed). Horizontal bars across the top show the lives of each of the identified loops; several of which are numbered. For convenience time axes are given for both hours after 00:00 Aug-10 and in conventional 24-hour notation. The top panel shows the GOES 1–8 Å channel, in W/m^2, for reference. The dashed line is 0.7×10^{-6} W/m^2, the approximate background level at this time.

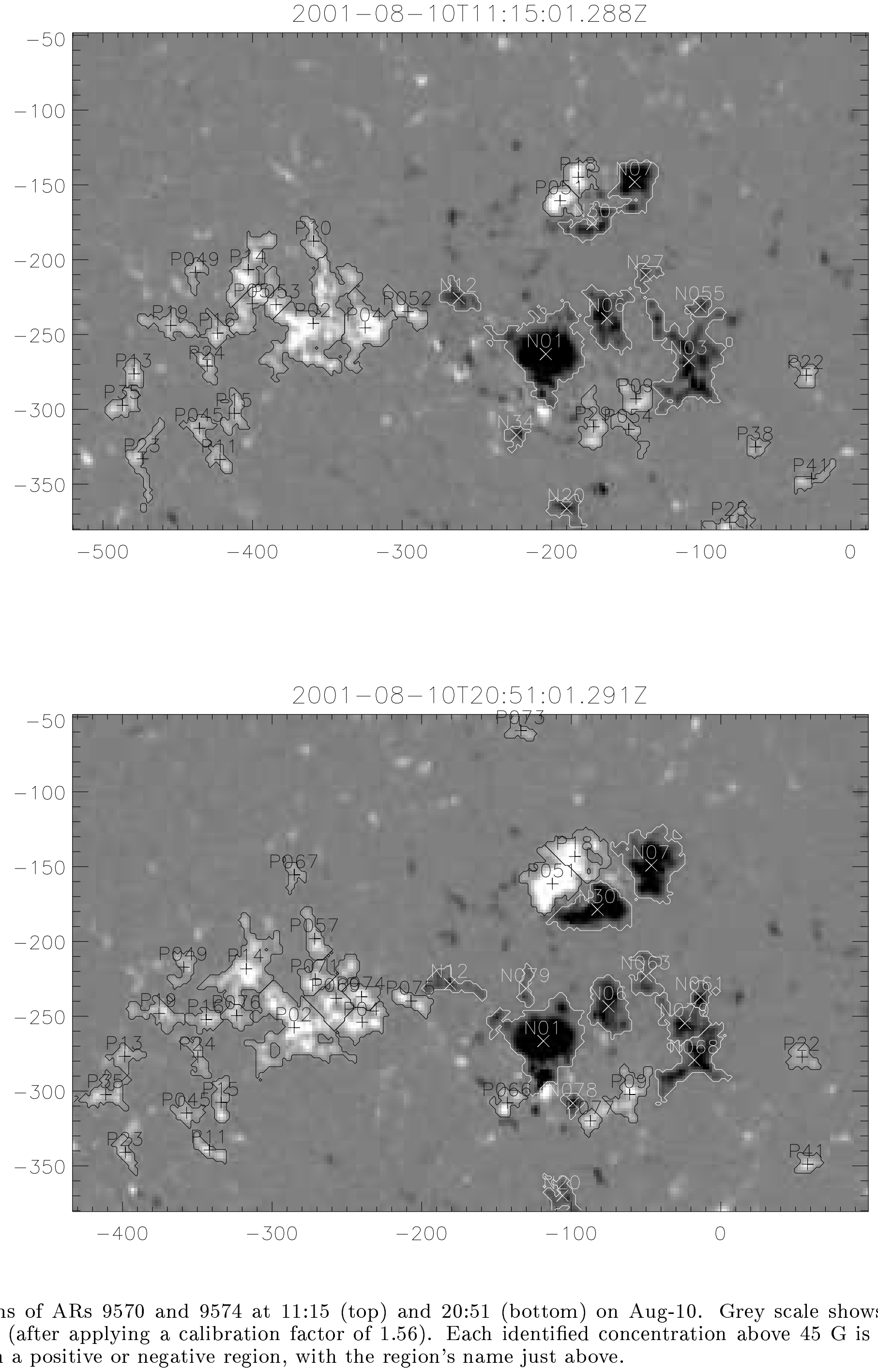

FIG. 8.— Magnetograms of ARs 9570 and 9574 at 11:15 (top) and 20:51 (bottom) on Aug-10. Grey scale shows the line-of-sight field strength between ±500 G (after applying a calibration factor of 1.56). Each identified concentration above 45 G is traced out. A + or × marks the center-of-flux in a positive or negative region, with the region's name just above.

factor under the assumption that the field is purely radial at the photosphere. There is a small but persistent imbalance between opposing polarities, even within the emerging active region. We do expect the more concentrated leading (negative) polarity to be favored by our thresholding procedure and possibly by the response of MDI (Berger & Lites 2003). To compensate for this we augment the fluxes in positive concentration by 7.5%. This seems to restore approximate flux balance to both active regions at the same time.

The corrected flux from each concentration is then assigned to a point charge located at the concentration's center-of-flux. This charge is then projected onto a tangent plane whose point of tangency is near the center of unsigned flux (the exact point is at 9.15° South, rotates at 13.5° per day, and crosses the central meridian at 15:41 on Aug-11). The leading polarity and only sunspot in the older active region AR 9570 is the largest concentration $N01$, which does not move appreciably over the entire period. The following polarity consists of numerous small positive concentrations which move about in a complex manner, occasionally appearing or disappearing; this does not, however, appear to correspond to any systematic motion. The emerging active region, 9574, consists of two positive concentrations, $P18$ and $P051$, and two negative concentrations, $N07$ and $N30$. These grow and separate during most of the observation. The flux-weighted midpoint of each polarity separate at an approximately constant rate of 215 m/sec along a line 8.4° south of West.

The largest flux concentrations include sunspots and very strong fields, to which MDI is known to be less sensitive. Our calculations will therefore underestimate the fluxes of the largest concentrations. There seems to be no accepted method for correcting this instrumental artifact, but it is possible to estimate its magnitude. Berger & Lites (2003) observe a weakened MDI response when the vertical field strength exceeds $B_{\rm sat} = 1700$ G and their calibration factor of 1.56 fits the instrument's response to fields weaker than this value. Using this same factor in strong field regions, as we have done, will undercount total fluxes there. The amount of undercounting can be estimated by integrating $|B_{\rm los}| - B_{\rm sat}$ over all pixels whose adjusted strength exceeds $B_{\rm sat}$. This integral is 4.1% and 4.5% of the total fluxes in regions N01 and P051 at the late time 17:39 on Aug-11 (P18, N07 and N30 have values between 0.7% and 1.7% of their total fluxes). If the sensitivity of MDI to fields stronger than $B_{\rm sat}$ were actually reduced by exactly one half, then these small factors would be the relative undercounting of the fluxes in each region. Plots in Berger & Lites (2003) indicate that the sensitivity is probably not reduced quite that much nor is the response really piece-wise linear. Thus we retain the values calculated with the uniform correction factor of 1.56 and bear in mind that the two largest sources, N01 and P051, are in reality larger than they are in our model, but probably by no more than a few percent.

The evolution of fluxes in the various concentrations is summarized in fig. 9. The three solid lines are the net flux in the positive polarity (top line) negative polarity (bottom line) and entirety of AR 9574 (net signed flux, middle line). The three broken lines give the same values for AR 9570. The middle lines show the extent to which the 7.5% correction has restored flux balance to each of the active regions. The flux in the older region, AR 9570, remains approximately constant, $\sim 1.2 \times 10^{22}$ Mx, while that in the emerging region increases beginning at $\sim$ 7:34 Aug-10. Even though some flux concentrations exist prior to 00:00 Aug-10, the emergence appears to begin in earnest only after 07:00. During the initial phase the flux in each polarity increases at approximately 122.4×10^{15} Mx/sec, shown by dashed lines. This linear fit intersects zero at 07:34, which we take to be the initiation of genuine flux emergence. Prior to this the flux in AR 9574 is poorly organized and does not increase very rapidly.

3.2. *The model*

The observations are used in a magnetic model for the effect of active region emergence. The dispersed nature of the following polarity of AR 9570 results in appearance and disappearance of identified concentrations, partly as an artifact of the thresholding and other processing steps. In order to focus on the emergence rather than these other, partly artificial effects, we freeze AR 9570 in the configuration from 17:20 on Aug-10. This configuration consists of 32 concentrations, 10 negative and 22 positive which represent the dispersed following plage. Each source is reduced to a total flux and centroid location on the tangent plane. The configuration is "frozen" in the sense that the fluxes remain constant and locations are fixed to the tangent plane, which itself rotates with the Sun. The four concentrations of AR9574, designated $P18$, $P051$, $N07$ and $N30$, vary in time according to the magnetograms. These four time-varying sources are added to the 32 sources from 9570 to produce the complete magnetic model.

The simplest model of the coronal field is a potential field extrapolated from the 36 point sources situated on the $z = 0$ plane. Source region i, with net flux Φ_i is modeled by a point source with magnetic charge $q_i = \Phi_i/2\pi$. Placing all sources on the same tangent plane guarantees that all flux from the upward-facing hemisphere of each charge enters the corona. The resulting potential field has 37 photospheric null points (also in the $z = 0$ plane), including one with a vertical spine, known as an *upright* null. The field lines in this model fall into 105 domains, according to which negative and positive sources they interconnect (Longcope 1996, 2001). Mapping fan and spine field lines from each of the null points produces a *skeleton* of the potential field (Bungey et al. 1996; Longcope & Klapper 2002), dividing it into its 105 domains. Figure 10a shows the footprint of the skeleton in the vicinity of the emerging active region. The dashed and solid curves, originating from each of five selected null points, divide the plane into 6 regions which are the footprints of 6 domains. One domain near the center consists of field lines connecting positive source $P051$ (one of the following sunspots in AR9574) to negative source $N01$ (the leading sunspot of AR9570). This domain is bounded by spines and fans from null points labeled $B1$ and $A2$, and shaded in fig. 10a.

In this potential field model source $P18$ (the northern positive sunspot in the emerging region) connects only to the negative sources in the same region (namely $N07$ and $N30$). The other positive source, $P051$, connects to these and also to $N01$ and $N06$ in the other active region. The negative sources in the emerging region connect via long

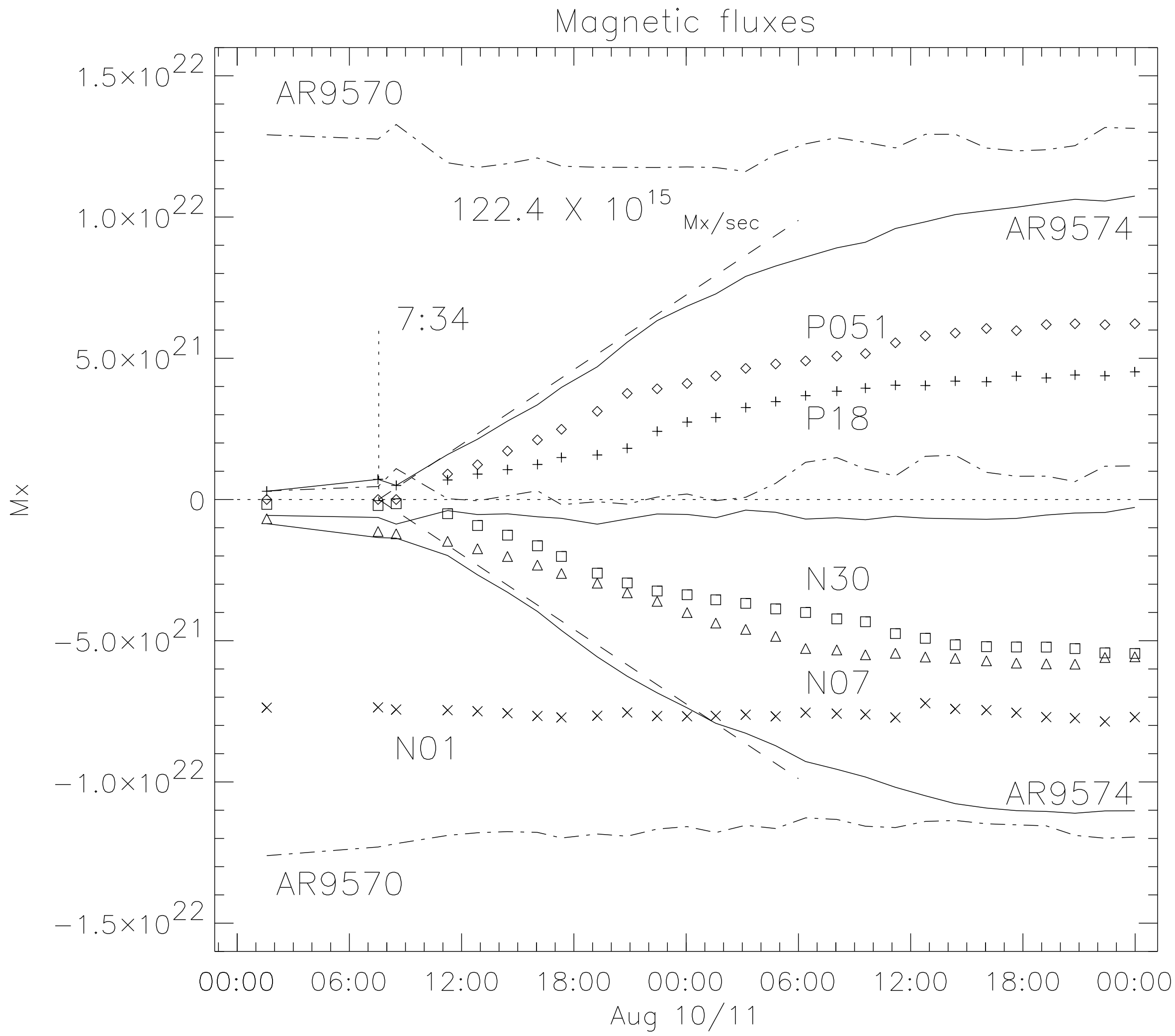

FIG. 9.— The evolution of flux in active regions 9574 (solid lines) and 9570 (broken lines) and several specific concentrations (symbols). The top and bottom line of each type are the total flux in positive and negative polarities respectively. The center line, hovering near zero, is the net signed flux in each active region.

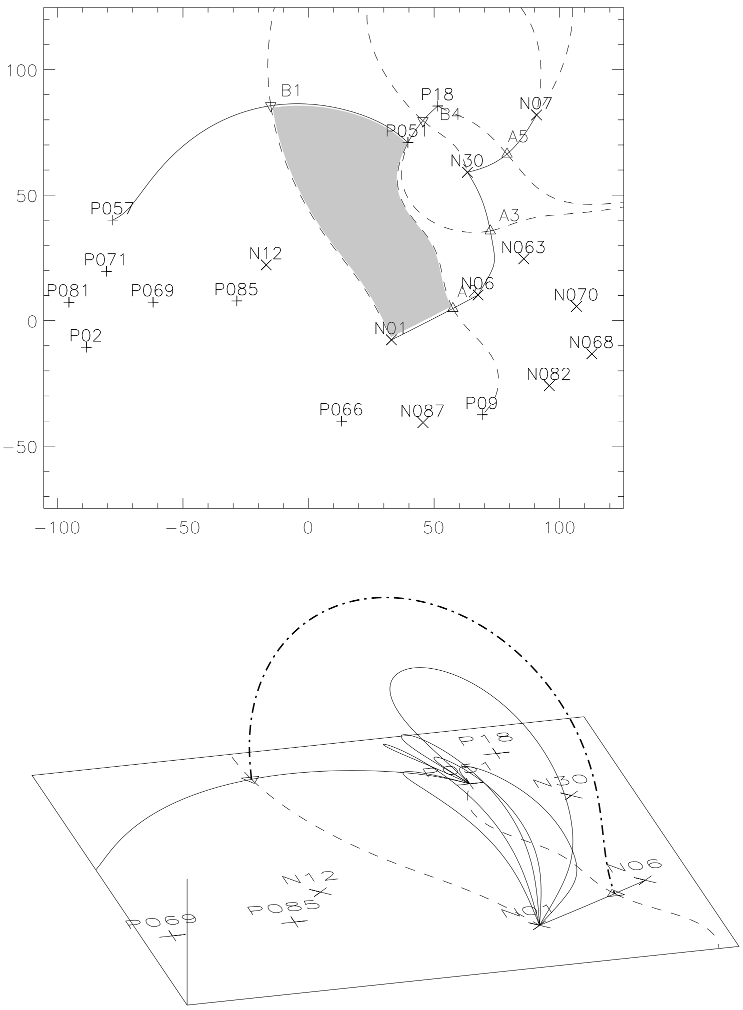

(a)

(b)

Fig. 10.— The potential magnetic field model at 22:27 on Aug-10. (a) The footprint of the skeleton showing locations of positive and negative sources as +s and ×s respectively. Five null points, labeled $B1$ – $A5$, are designated by triangles (△ and ▽ for negative (B) and positive (A) null points). Dashed curves are the photospheric portion of the fans and solid lines are the spines. The shaded region is the footprint of domain $P051$–$N01$. (b) Perspective view of field lines belonging to domain $P051$–$N01$ (thin solid curves). The thick dash-dotted line is the separator linking null points $B1$ to $A2$.

arching field lines to numerous small sources in the following plage of AR9570. Of these interconnecting domains we focus on $P051$–$N01$ since it is by far the largest and appears to be the domain of the observed loops. The bottom panel of fig. 10 shows a perspective view of some representative field lines from this domain.

Domain $P051$–$N01$ is enclosed by the fan surfaces of null points $B1$ and $A2$. This the shaded region of the footprint of the potential field (fig. 10a) where the domain is bounded by fan traces (dashed) and spine field lines (solid) from each null. This structure is, however, topologically robust and will persist in any non-potential field in which the domain $P051$–$N01$ is present. In all such fields the fans extend upward into the corona forming a tent above the domain. The tent's ridge-line is formed by the separator where the two fan surfaces intersect. In the potential field the separator is the single field line running from null point $B1$ to null point $A2$.

Because of its location at the ridge of the enclosing tent, the separator encloses all field lines from domain $P051$–$N01$ and no others. A curve within the separator, directed from $B1$ to $A2$ may be closed along the photosphere to form a circuit $\mathcal{Q}$. (It must be recalled that while the the separator of a potential field is a single field line, in a general field it may be a ribbon of field lines (Longcope & Cowley 1996).) Integrating the vector potential $\mathbf{A}$ along this circuit gives the total flux interconnecting sources $P051$ and $N01$ (Longcope 1996; Longcope & Klapper 2002)

$$\psi \;=\; \int_{\mathcal{S}} \mathbf{B}\cdot d\mathbf{a} \;=\; \oint_{\mathcal{Q}} \mathbf{A}\cdot d\mathbf{l} \quad , \tag{2}$$

where $\mathcal{S}$ is some surface bounded by $\mathcal{Q}$. Performing this integral for the *potential* field generated from the point-source model of the MDI magnetograms yields a flux $\psi^{(\mathrm{v})}(t)$ as a function of time. This time-dependent function, plotted in fig. 11, is negative since the field lines pass under the separator in the negative sense: following the separator from $B1$ to $A2$ with the fingers of the left hand the field is directed along the the thumb, toward the south. Throughout the emergence process, approximately one-third of the flux from $P051$ connects to $N01$ in the potential field; most of the rest remains within AR9574, connecting to $N07$ or $N30$.

While the actual coronal field may differ from the potential model it will nevertheless have a separator from which an isolating loop $\mathcal{Q}$ may be constructed. As in the potential model, all interconnecting flux must pass through $\mathcal{Q}$, and expression (2) will yield the total interconnecting flux. The amount of interconnecting flux can change only if a loop voltage

$$\frac{d\psi}{dt} = -\oint_{\mathcal{Q}} \mathbf{E}\cdot d\mathbf{l} \quad , \tag{3}$$

is produced along the circuit $\mathcal{Q}$. In principle there could be a contribution to (3) from an electric field along the photospheric leg of $\mathcal{Q}$. This contribution would arise from $\mathbf{v}\times\mathbf{B}$ as flux crosses the photosphere corresponding to the emergence of field lines already interconnecting the different active regions. Since the positive and negative poles of AR9574 increase together it seems likely that all emerging flux takes the form of a classic flux tube interconnecting the region's two polarities. For this reason we reject the possibility and thereby assume that the full voltage drop occurs along the coronal separator.

Rejecting the possibility that interconnecting field lines were created through emergence leaves only the possibility of separator reconnection manifest as a parallel electric field along the separator. As the potential field evolves it undergoes kinematic reconnection across the separator (Greene 1988; Lau & Finn 1990). In this reconnection field lines from domain $P057$–$N01$ of AR9570 and field lines from $P051$–$N06$ approach the separator. Field lines from each domain meet at the separator, break and are rejoined with swapped ends to form new field lines in domains $P051$–$N01$ and $P057$–$N06$. It is the former field lines which augment the flux in the interconnecting domain. The theory requires that for each such field line added to $P051$–$N01$ one must also be added to $P057$–$N06$. Reconnection in the actual coronal field must be topologically equivalent to this, although the separator may be deformed into a ribbon of finite width (Longcope & Cowley 1996).

Our analysis replaces each of the observed flux concentrations with a magnetic point source. A point source located at the centroid (and within the $z = 0$ plane) is the leading term in a multipole expansion of the potential field from the extended source region. The use of point sources, while convenient, is not essential for the topological analysis. The same topology described above would be found if the photospheric field were extrapolated directly from the extended source regions (Longcope 2001). Separatrices, for example, are surfaces separating field lines with distinct footpoint locations. As long as the photospheric field consists of distinguishable regions the coronal field will have separatrices. The crucial step in establishing a topology is, therefore, the division of the photosphere into distinct regions. In particular the separation of flux belonging to AR 9574 from that belonging to AR 9570. As long as such a separation is possible there will be separatrices, a separator and the possibility of separator reconnection exactly as described above.

4. QUANTIFYING THE RECONNECTION

The TRACE data presented in §2 provide clear observational evidence of flux in the $P051$–$N01$ domain which, as the previous section argued, must result from separator reconnection. To quantify this reconnection we will use the observations to estimate the total amount of interconnecting flux. Doing so requires four basic assumptions, which we number as an aid to future discussion. 1. We assume that each of the 43 identified loops is a bundle of field lines, also called a flux tube, from domain $P051$–$N01$. 2. We assume the loops, and therefore also the flux tubes, have circular cross sections whose diameters are the full width at half maximum found in the 171Å images. 3. We assume that over its observed duration a given coronal loop tracks a single flux tube. 4. We assume that no flux tube re-appears in 171Å, and thus that every identified loop represents a different interconnecting flux tube.

The assumed correspondence between observed coronal loops and model flux tubes is illustrated by Figure 12. The TRACE image shows a particular loop (loop 4) crossing the slit (solid horizontal line) and the footprint of the model field in red. The first point worthy of note is that the fan surfaces of both $B1$ and $A2$ (dashed lines) cross the slit; and that the coronal loop crosses between them.

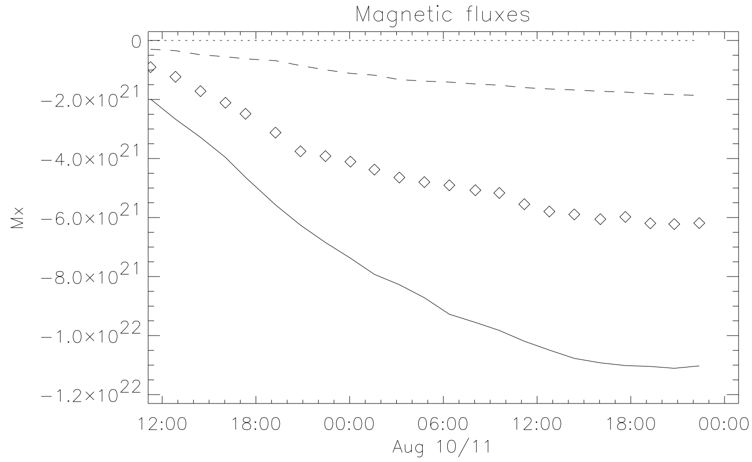

FIG. 11.— The total flux connecting $P051$ to $N01$, $\psi^{(\mathrm{v})}(t)$ (dashed line). The solid line is the total flux in the negative polarity of AR9574, as shown in fig. 9. The diamonds are the negative of the flux in source $P051$.

The time evolution of the potential-field fan surface crossing points are plotted as dashed curves in both stack plots 2 and 4. As the domain flux, $\psi^{(\mathrm{v})}$, grows, the separatrices expand causing the crossing points to separate. Almost all observed loops, when projected along the line of sight, fall between the separatrices of the potential-field domain $P051$–$N01$, giving credence to assumption 1: loops appear to be associated with field lines in the $P051$–$N01$ domain.

A flux tube in domain $P051$–$N01$ is selected to resemble loop 4. To do this, model field lines are integrated from various points along the line-of-sight defined by the intersection of loop 4 and the slit. One starting from a height of $z = 33$ Mm, is selected due to its resemblance to the the overall shape of the loop (see bottom panel of fig. 12). The characteristics of this field line and of the separator are summarized in fig. 13. At the slit-crossing point (diamond) the field line has strength $|\mathbf{B}| = 37$ G and loop number 4 has diameter (full width at half maximum) $d = 2.6$ Mm (panels (d) and (e) respectively). A circular flux tube with this diameter encloses a total flux $\Phi = 2.0 \times 10^{18}$ Mx.

More generally, a field strength B_0 at the slit-crossing implies that a tube whose apparent diameter is d has flux $\Phi = (\pi/4)d^2 B_0$. The 43 observed loops have median diameter $d = 3.7$ Mm, corresponding to a flux $\Phi = 4 \times 10^{18}$ Mx if the field strength were $B_0 = 37$ G as it is for the potential-field model of loop 4. The fact that all of the reconnected flux seen at 171Å takes the form of loops with very similar diameters suggests a sporadic or patchy reconnection transferring flux in parcels of $\sim 4 \times 10^{18}$ Mx at a time.

The total flux transferred by all 43 flux tubes will be $\Delta\psi \simeq 43\Phi = 1.7 \times 10^{20}$ Mx. Accumulating the cross sectional area of the actual loops and attributing each to the time of its first appearance generates the area curve $A(t)$ shown in fig. 14. The curve jumps by $(\pi/4)d^2$ at the onset of each loop brightening. The duration of that loop is indicated by a horizontal line beginning at the jump. The curve rises quite gradually until 9:00 Aug-11, when a flurry of loop brightenings causes it to rise at $\dot{A} \simeq 3.9 \times 10^{14}\,\mathrm{cm}^2/\mathrm{sec}$ for a three-hour interval.

The flurry of brightenings persists for approximately 3.5 hours, transferring $\sim 2 \times 10^{19}\,\mathrm{cm}^2$ of accumulated area. The plot in fig. 14 uses a less conservative field strength of $B_0 \simeq 120$ G, since it is the largest value we consider plausible, makes the plot clearer and helps illustrate further discussion. With this larger value $\Delta\psi \simeq 5 \times 10^{20}$ Mx of flux is transfered in 3.5 hours (the minimum possible value, $B_0 = 37$ G gives only one third this much). These observed flux transfers can be compared to the potential field values, $\psi^{(\mathrm{v})}(t)$ (the dashed line) whereby $\simeq 1.5 \times 10^{21}$ Mx is transferred steadily over 36 hours, at an average rate of 11.6×10^{15} Mx/sec. The observed loops account for between one-ninth and one-third of this transfer rate, depending on B_0 the assumed field strength in the tubes. The peak transfer rate exceeds the average rate at which a potential field would transfer flux by as much as a factor of three.

The loop observations can also be used to quantify the energy input into the plasma. The density lower bound n_e puts a lower bound on radiative power density

$$\mathcal{P}_r = \alpha_{\mathrm{Fe}} n_e^2 \Lambda_0 \quad , \tag{4}$$

where α_{Fe} parameterizes the relative abundance of iron and the radiative loss function has been approximated as $\Lambda(T_e) \simeq \Lambda_0 = 10^{-21.94}\,\mathrm{erg\,s^{1-}cm^3}$, a constant over the peak TRACE response $0.5\mathrm{MK} < T_e < 2.0\mathrm{MK}$ (Rosner et al. 1978; Aschwanden et al. 2003). The radiative power density defines a radiative cooling time $\tau_{\mathrm{rad}} \equiv 3n_e k_{\mathrm{B}} T_e/\mathcal{P}_r$, which will be an upper bound on the expected life time of a freely cooling loop since our density estimates are themselves lower bounds. The 171 Å response has half its peak value within the range $0.65\mathrm{MK} < T_e < 1.25\mathrm{MK}$, so the duration within this band should be a factor $\ln(1.25/0.65) = 0.65$ of the cooling time.

Figure 15 shows the observed duration of loops versus their density lower bounds. Assuming even modest iron enhancement, $\alpha_{\mathrm{Fe}} = 2$, yields a cooling life-time shorter than most observed durations. With no enhancement at all, $\alpha_{\mathrm{Fe}} = 1$, more than a third of the loops last longer than the upper bound on their cooling life-time. For the value taken as typical of active region loops, $\alpha_{\mathrm{Fe}} = 4$ (Aschwanden et al. 2003), every single loop lives longer than its radiative lifetime. All of these comparisons suggests

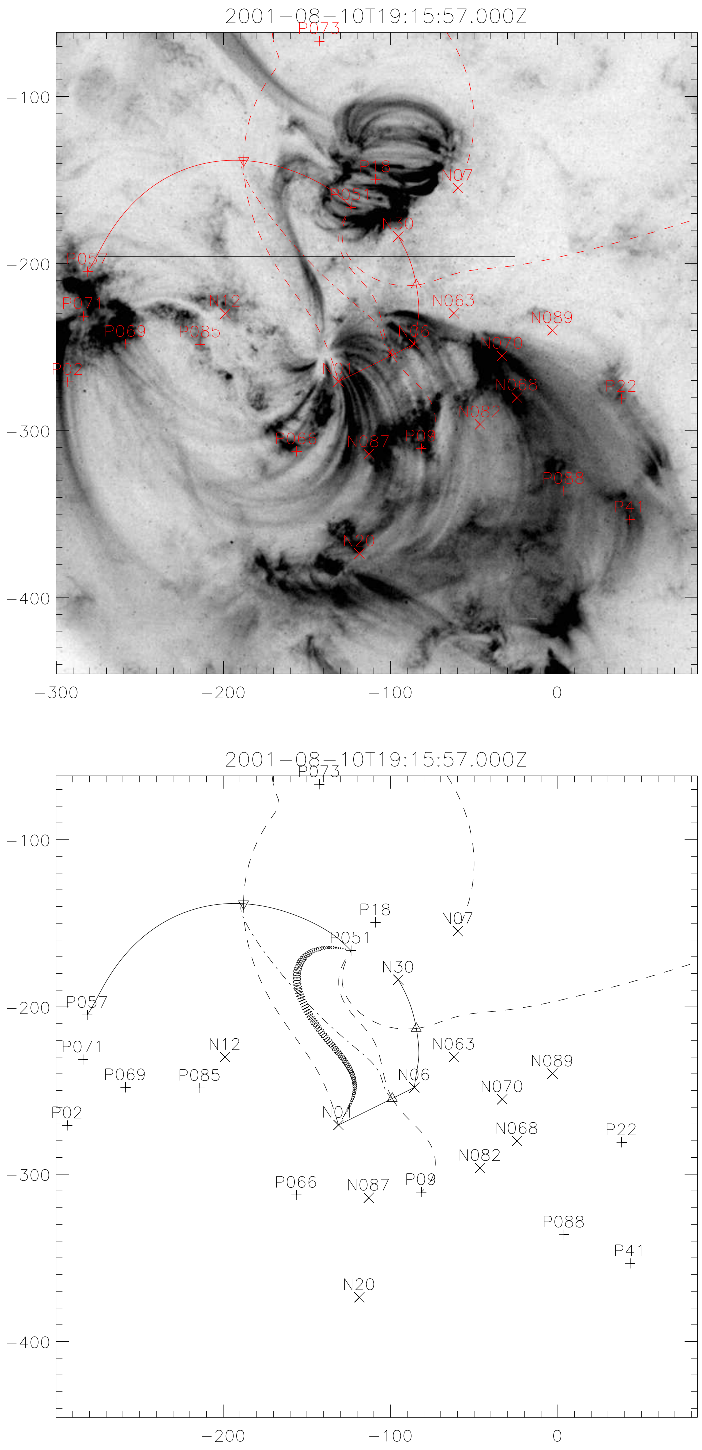

FIG. 12.— Correspondence between an identified coronal loop (loop 4) observed at Aug-10 19:15, and a field line from domain $P051$–$N01$ in the magnetic model from the same time. (top) A superposition of the TRACE image (grey scale) and the footprint of the field (red lines). The black horizontal line is the slit at that time. (bottom) The footprint and a flux tube from domain $P051$–$N01$ (dark curved feature).

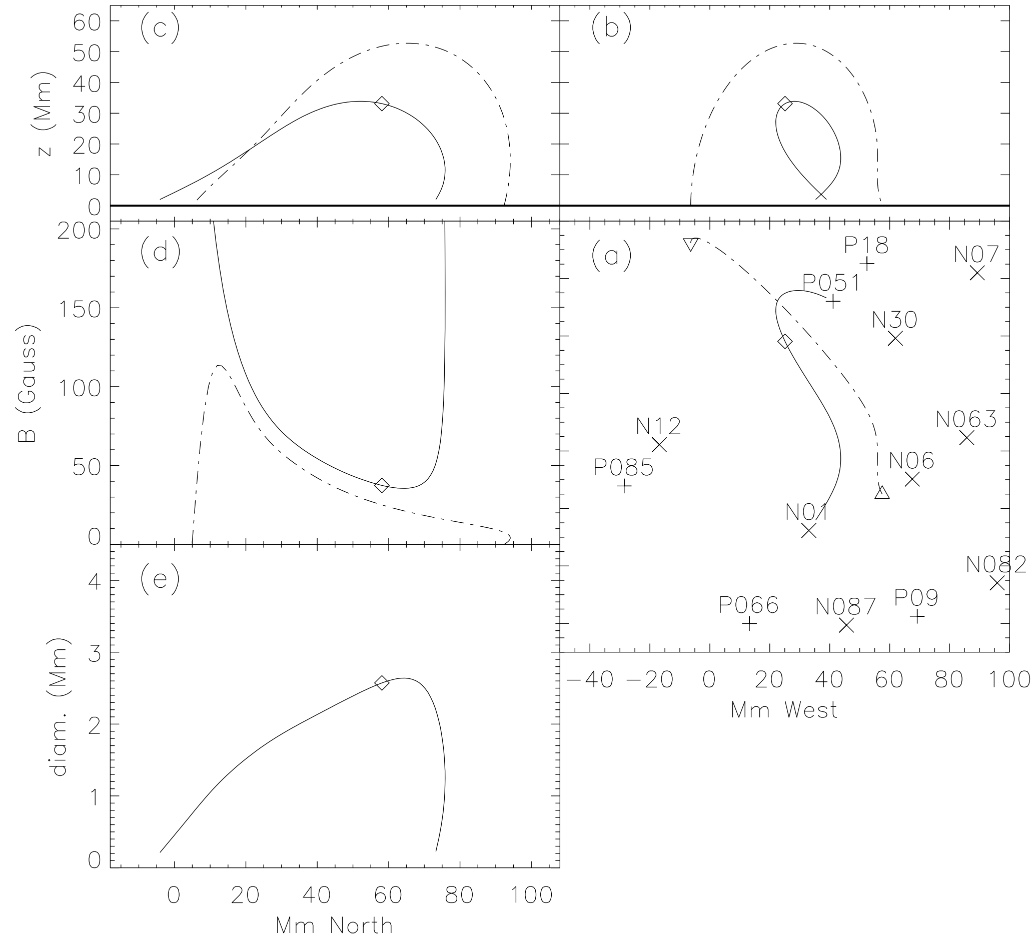

FIG. 13.— A field line selected to model loop 4 at 19:00 on Aug-10. Each panel shows the field line (solid), the separator (dash-dot) and the point of slit-crossing (diamond). The different plots are, reading counter-clockwise from lower right: (a) A view from above the tangent plane showing the neighboring sources. Elevations as seen from a viewpoint (b) the the South and (c) the East. Plots of the loop properties as a function of the y coordinate showing (d) the magnetic field strength and (e) the flux tube diameter.

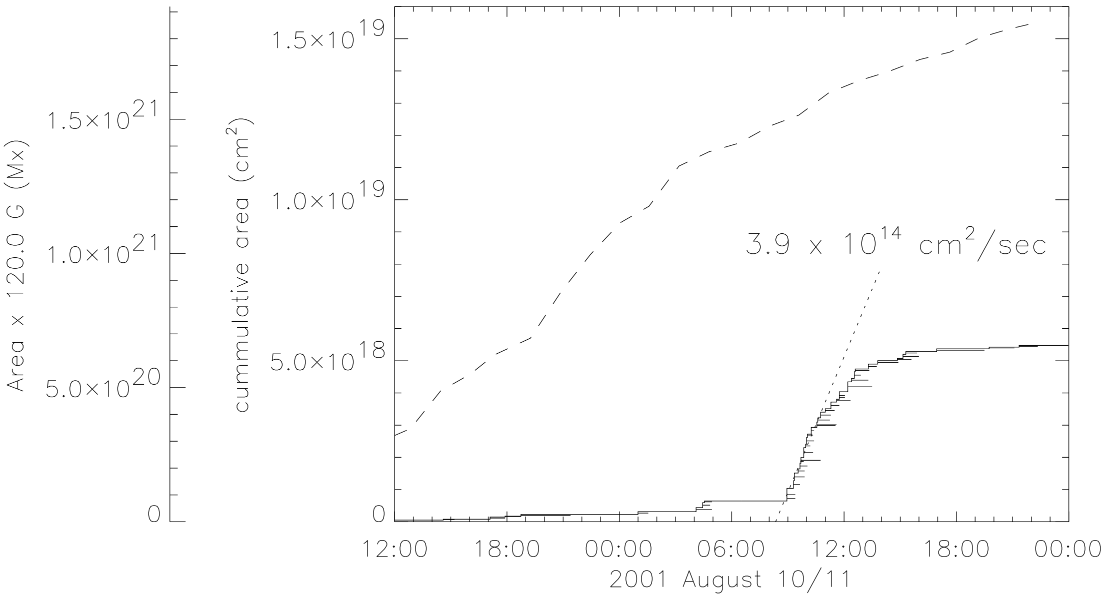

FIG. 14.— The accumulated areas of coronal loops $A(t)$ (solid curve). The curve jumps by $(\pi/4)d^2$ at the initiation of each loop. A horizontal bar from that point indicates the duration of that loop. A second axis gives the equivalent flux assuming a field strength of $B_0 = 120$ G. The dashed curve shows the interconnecting flux in a potential model, $\psi^{(\mathrm{v})}(t)$, on the flux axis.

that loops are undergoing some heating throughout their period of 171Å emission. It is also noteworthy that the density lower bounds all exceed the apex density of a 120 Mm loop in equilibrium according to Rosner, Tucker and Vaiana (RTV, Rosner et al. 1978).

Concurrent observations from the *Yohkoh* SXT provide further insight into the energetics of the reconnected loops. Interconnecting structure can be discerned as early 11:48 on Aug-10, two hours prior to the appearance of Loop 1 in the 171Å data. A generalized brightening over the entire active region complex begins at 5:23 on Aug-10. Shortly after this there is a very bright knot in the center of the reconnection region (see fig. 16). By 7:13 this resolves into a single wide loop-like structure within the $P051$–$N01$ domain, which remains pronounced and bright for ~ 3 hours.

Partial frame images (PFIs) of the region were made at high time-cadence mostly during two intervals. These alternate between filters and therefore may be used to derive temperatures and emission measures. Figure 17 shows the total emission measure and average temperature in each of two distinct regions. Region A includes only the bright E-W loops forming AR 9574; these are the horizontal features centered at $x \simeq 20$", $y \simeq -170$" in fig. 16. Region B includes all features in the interconnecting domain. The emission measure and temperature of region A stay roughly constant at $EM \simeq 0.5\times 10^{48}\,\mathrm{cm}^{-3}$ and $T \simeq 6$ MK. The emission measure of region B is clearly increasing in the first PFI set (beginning at 5:46) and decreasing by the second set (beginning at 9:04). The temperature of region B is above 7.5 MK during its rising phase and has fallen to the same value as region A (~ 6 MK) by the second interval. Indeed, the average temperature of region B at 9:15 appears to be steadily falling at a rate $dT/dt \simeq -0.6$ MK/hour (the fit shown as black dotted line), in contrast to region A which appears to be maintaining its 6 MK temperature. All of this is consistent with the scenario that reconnection begins some time after 4:30, and that the reconnected loops (region B) cool gradually over the next 6–8 hours.

We conclude that region B primarily includes emission measure from the reconnected flux. The volume of a reconnected flux tube is the product of its flux $\Delta\psi$ and the integral

$$\mathcal{V} \equiv \int \frac{d\ell}{|\mathbf{B}(\ell)|} \quad , \tag{5}$$

over the axis of the tube. For a field line selected in a manner similar to fig. 13, but at 7:00 on Aug-11, we find $\mathcal{V} = 1.0$ Mm/G. If the peak emission measure, $EM = 1.9\times 10^{48}\,\mathrm{cm}^{-3}$, corresponds to the entirety of the reconnected flux from fig. 14, $\Delta\psi = 6\times 10^{20}$ Mx, then it would occupy a volume $V = 6\times 10^{28}\,\mathrm{cm}^3$ at an average density of

$$n_e = \sqrt{\frac{EM}{V}} = \sqrt{\frac{EM}{\Delta\psi\mathcal{V}}} = 5.6\times 10^9 \quad . \tag{6}$$

Had we used a more conservative estimate of the emitting magnetic flux, $\Delta\psi$, the density estimate would be even higher. Comparison to the 171 Å density estimates indicate that the loops drain to a much lower density by the time they pass through the TRACE pass band, beginning at 9:00.

At the very high temperatures observed by SXT, the dominant cooling will be by thermal conduction. The conductive cooling time

$$\tau_{\mathrm{cond}} \equiv \frac{3n_e k_{\mathrm{B}}(L/2)^2}{\kappa_0 T^{5/2}} \quad , \tag{7}$$

will be 1000 seconds (0.3 hours) for a $T = 6$ MK plasma at the density just derived. In spite of this, the loops persist for 4–5 hours before fading from SXT and appearing in TRACE. Moreover, the observed cooling rate at

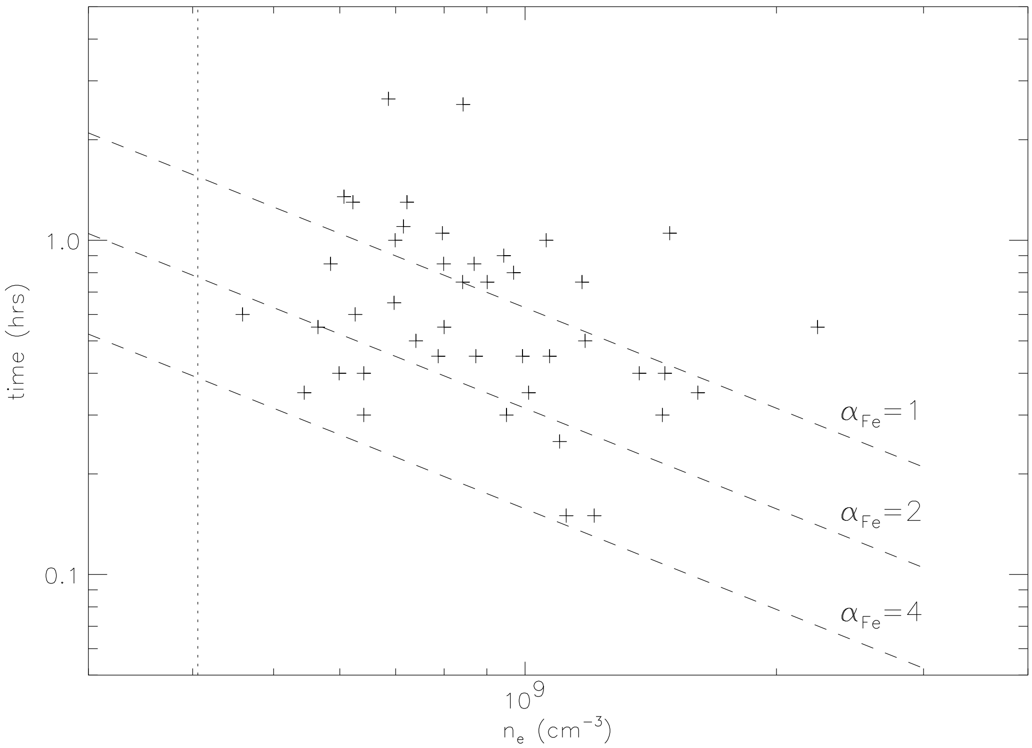

FIG. 15.— A plot of the observed duration of each loop against the lower-bound estimate on its average density, n_e. The dashed lines are $0.65\tau_{\rm rad}$ for values of the iron abundance $\alpha_{\rm Fe} = 1$, 2, and 4. The vertical dotted line is the apex density of a coronal loop in RTV equilibrium.

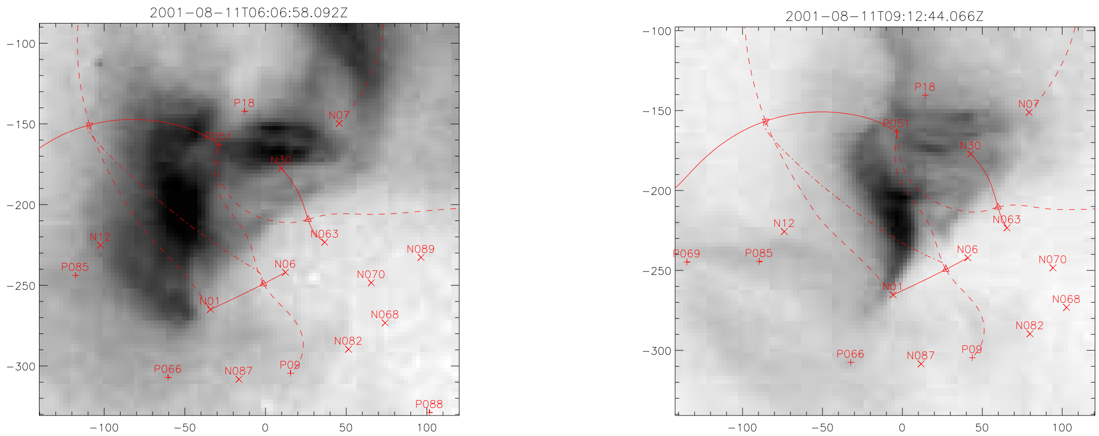

FIG. 16.— Partial frame images from *Yohkoh* SXT at 6:06 (left) and 9:12 (right) on Aug-11. The inverse grey-scale is square-root of intensity (to enhance contrast). Features of the magnetic model are over-plotted as in fig. 12.

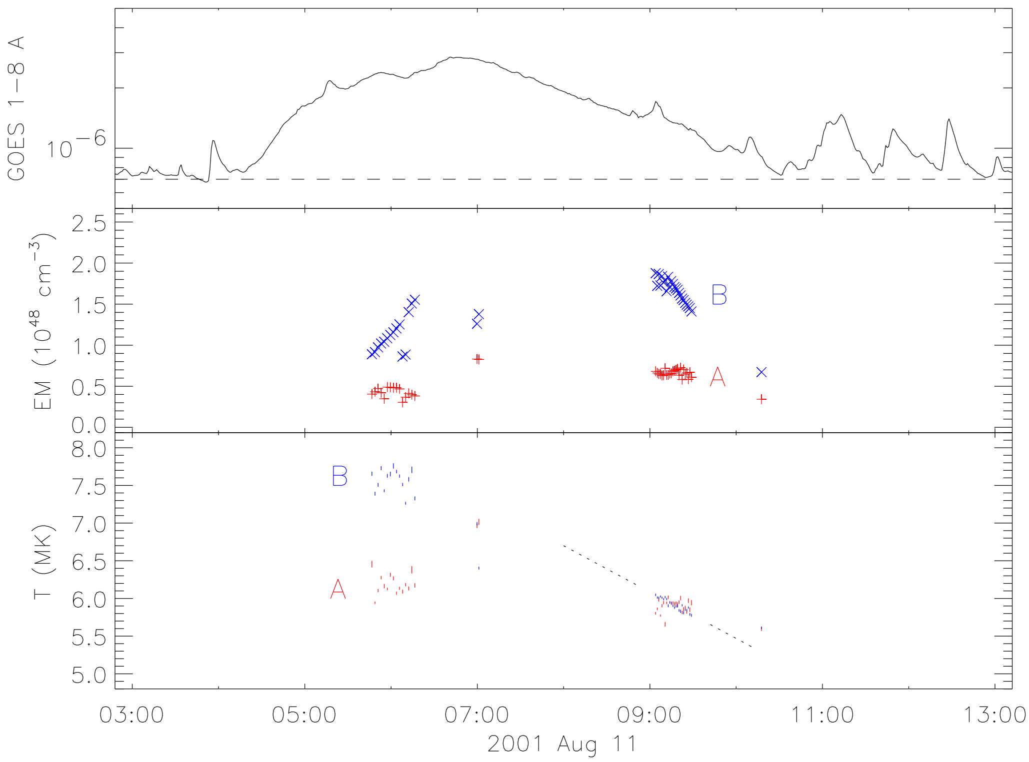

FIG. 17.— Time histories of X-ray-derived quantities at the reconnection episode. The top panel is a section of the same GOES curve from fig. 7. The middle panel shows the total emission measure in region A (red +, AR 9574) and region B (blue ×, interconnecting flux) in units of $10^{48}\,\mathrm{cm}^{-3}$. The bottom panel shows the average temperatures of the same two regions as vertical error bars denoting the uncertainty. A black dotted line shows a fit to the late cooling trend of region B, $dT/dt = -0.6$ MK/hour.

9:15 (see fig. 17) gives an instantaneous cooling time of 10 hours. This slow cooling strongly suggests there is continued heating for considerable time after the reconnection has occurred.

Over this same period the GOES 1–8 Å channel, shown along the tops of figs. 7 and 17, rises from its background level $F_{\rm bg} \sim 7.5\times10^{-7}\,\mathrm{Watts\,m^{-2}}$. The rise begins at about 4:30, reaching a peak of $F \simeq 3\times10^{-6}$ at 6:45 and then returning to the background level at 10:30. We propose that the 5:00–7:00 period of rising X-ray emission corresponds to the episode of separator reconnection transferring the flux visible at 171Å 4 hours later, at 9:00. The reconnected flux tubes are filled with very hot plasma which gradually cools, passing first through SXT and then TRACE passbands.

The energy released by reconnection can be estimated from both the EUV and X-ray observations. The total power radiated in all wavelengths is $\mathcal{P}_r$ times the volume V of the loop, where $\mathcal{P}_r$ is taken from expression (4). The total energy needed to keep the loop bright in EUV for τ_{171} is

$$\Delta E \;=\; \mathcal{P}_r V(\tau_{171} - \tau_{\rm rad}) \quad , \tag{8}$$

where $\tau_{\rm rad}$ is its radiative cooling time, here taken with iron enhancement $\alpha_{\rm Fe} = 4$ following Aschwanden et al. (2003). The median energy release from the 30 loops brightening between 9:00 and 12:00 is $\Delta E = 6\times10^{26}$ erg; the sum of all 30 energies is $\sum\Delta E = 3.5\times10^{28}$ ergs. Since $\mathcal{P}_r$ is found using a lower bound on the electron density n_e, this value is a lower bound on the energy radiated by these interconnecting loops during their appearance in 171 Å.

An alternative estimate of the radiated energy comes from the GOES light curves in both the 1–8 Å (see fig. 17) and the 0.5–4 Å channels. The pre-event flux (background) of disk-integrated X-rays was approximately 7.5×10^{-7} W m^{-2} and 1.2×10^{-8} W m^{-2} in the two channels respectively. Peak flux occurred near 06:45 UT in both channels: 3.4×10^{-6} W m^{-2} and 4.4×10^{-7} W m^{-2}. Using GOES analysis software in SolarSoft (Freeland & Handy 1998) a ratio of the channels is compared to the response functions of the GOES instrument to estimate the plasma temperature (Thomas et al. 1985; Garcia 1994) at between 5 MK and 7 MK during the interval of elevated X-ray flux. Based on a synthetic solar spectrum, these temperatures indicate emission measures in the range 2–10 × 10^{48} cm^{-3}; this is larger than the SXT value. Integrating over the entire spectrum and over the interval 02:00 UT to 11:00 UT gives a total radiated energy of 2.4×10^{30} ergs.

4.1. *Modeling energy storage and release*

The potential flux, $\psi^{(\rm v)}$, is generally taken as an upper bound on the flux which could be reconnected (Longcope 1996). When the observed loop areas are multiplied by the field strength from potential field, $B_0 = 37$ G, they account for much less than this upper bound. This could result from any combination of three basic factors. Either the reconnection has transferred less flux than necessary to achieve a potential field, or the flux tube fields are stronger than in the potential extrapolation, or some portion of the reconnected flux is too hot or too faint to be apparent in 171 Å data. The third possibility allows for the largest flux transfer since it is consistent with the flux-transfer upper bound $\psi^{(\mathrm{v})}$. Assuming this in an estimate of reconnection energy release yields the largest possible value, although the estimate itself is a lower bound.

Toward this end we assume that only a fraction f of the flux transfered after 12:00 Aug-10 is ever visible in 171 Å. To account for the observed cooling delay between SXT and TRACE 171Å we advance the cumulative area function by $\Delta t = 3$ hours. We find that multiplying the areas by $B_0/f = 250$ G produces a reconnection curve which achieves the potential value, $\psi^{(\mathrm{v})}(t)$, following the episode at 6:00 Aug-11 (see fig. 18). The interconnecting flux prior to this episode is smaller than $\psi^{(\mathrm{v})}$ by $\Delta\psi \simeq 1.1 \times 10^{21}$ Mx. We will estimate the energy which could be released by a reconnection episode which transfers this flux in three hours. Such a transfer would require a loop voltage $\dot{\psi} = 1.0 \times 10^{17}$ Mx/sec, or 10^9 Volts.

The potential field is the minimum energy state for a given distribution of photospheric flux. The fact that domain $P051$–$N01$ has flux different from $\psi^{(\mathrm{v})}$ means that the field cannot be potential (i.e. it must contain current). The minimum energy state subject to this single observational constraint, the actual flux ψ interconnecting $P051$–$N01$, is the *flux constrained equilibrium* (Longcope 2001). This equilibrium is current-free except for a current sheet running along the separator. Large-scale properties of this current sheet, such as width and net current, may be estimated using an expansion about the potential field (Longcope & Silva 1998; Longcope & Magara 2004). (The current density and thickness of the current sheet, on the other hand, would be set by *dynamics* in its vicinity and cannot be predicted using this or any quasi-static model.) In the potential field at 6:00 Aug-11 the separator B1–A2 is $L = 206.4$ Mm long and has an average shear parameter $I^\star/c = 2.4 \times 10^{11}$ Mx cm (2.4×10^{12} Amps), found by integrating the perpendicular magnetic shear along the separator of the potential field (see Longcope & Silva 1998; Longcope & Magara 2004, for details). In order to produce a self-flux compensating for $\Delta\psi$ the current sheet must carry a current I satisfying the equation (Longcope & Silva 1998; Longcope & Magara 2004)

$$\Delta\psi \;=\; \frac{IL}{c}\ln(eI^\star/|I|) \quad , \tag{9}$$

where $e = 2.718$ is the base of the natural logarithm, L is the length of the potential separator and $I^\star$ is its average shear parameter. The solution for the values given above is $I = 0.056\,I^\star = 1.34 \times 10^{10} c$ (1.34×10^{11} Amps).

Due to the flux constraint, this equilibrium has energy greater than the potential field by

$$\Delta W_{\mathrm{FCE}} \;=\; \tfrac{1}{2}L(I/c)^2\ln(\sqrt{e}I^\star/|I|) \;=\; 1.4 \times 10^{31}\,\mathrm{ergs} \quad . \tag{10}$$

Since the actual magnetic field is probably subject to constraints in addition to the one on its interconnecting flux, such as line-tying constraints, ΔW_{FCE} will be a lower bound on the free energy. Each additional constraint will store additional energy, and eliminating the constraint would release this stored energy.

The free-energy estimate in eq. (10) follows from the application of a single constraint to the coronal magnetic field. Additional energy ΔW_{FCE} is required because the total interconnecting flux, ψ, differs from the amount a potential field would have, $\psi^{(\mathrm{v})}$. The state of minimum energy has an infinitely thin current sheet, however, this does not mean, nor do we assume, that the actual magnetic field has a current sheet. The fact that the state of minimum energy contains a current sheet may suggest that the self-consistent dynamics of the coronal field will tend to concentrate current in the vicinity of the separator. Self-consistent, non-linear dynamics would ultimately determine details of the current distribution such as its thickness (resisitivity, for example, would prevent the formation of a genuine discontinuity). This is, however, a subject far too complex to delve into here. The salient point is that any coronal field with interconnecting flux ψ must contain magnetic energy in excess of the potential field by at least the amount in expression (10), where the current I is set by the flux discrepancy through (9).

5. DISCUSSION

The foregoing observation of the emergence of AR9574 has provided new insight into the process of magnetic reconnection in the corona. These insights follow after the data are interpreted in the context of a magnetic model. The interpretations are not always unambiguous so some of the results define ranges of possible values.

The simple presence of the interconnecting flux is, by itself, very strong evidence for separator reconnection. Assuming the interconnecting field has not emerged at the same time as the flux internal to AR9574, it must be created in the corona by exchanging the footpoints in pairs of field lines: reconnection. This process can only occur through some version of separator reconnection which is the topological analog of X-point reconnection in two dimensions (Longcope & Cowley 1996). The locations of the observed loops, their low densities, their inferred cooling and the observed energy release all argue against interconnected emergence and therefore in favor of separator reconnection.

The separators in our magnetic model occur because of the distinction we make between the two active regions. Some magnetic models, on the other hand, assume the photospheric magnetic field to be a monolithic, smooth function which cannot be unambiguously divided into regions. This approach eliminates all separators of the type discussed since it prevents categorical distinctions between footpoints. In their place are neighborhoods of distorted field-line mapping known as quasi-separatrix layers (QSLs) which are geometrical rather topological features (Priest & Démoulin 1995). In model problems where the photospheric field is changed from monolithic to discrete the QSLs in the first case are found to occur at the locations corresponding to the separatrices in the second (Titov et al. 2002). In this sense distinction between active regions might be considered as an approximation used to facilitate the identification of QSLs.

Real active regions do, however, appear to be distinct from one another in many physically meaningful senses. The process of active region emergence, of which AR9574 is one example, suggests a distinct entity has risen from an interior layer (Fisher et al. 2000). It is therefore quite natural to adopt a model which distinguishes magnetic footpoints in one active region from those in another. The

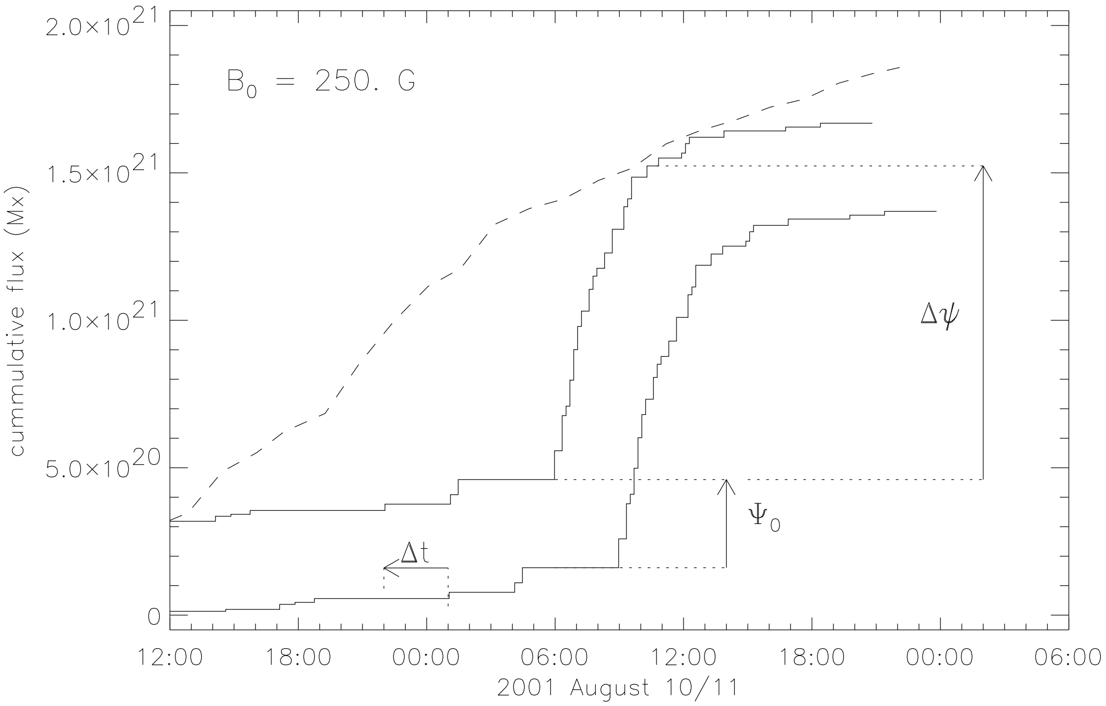

FIG. 18.— A plot of the accumulated loop area multiplied by $B_0/f = 250$ G (lowest curve) and the interconnecting flux in a potential field $\psi^{(v)}$ (dashed). The upper solid curve accounts for a cooling delay and possible unobserved early reconnection by advancing the observations by $\Delta t = 3$ hours and adding $\Psi_0 = \psi^{(v)}(12:00)$ to them. The resulting curve reaches $\psi^{(v)}$ following a reconnection episode occurring at 6:00. The extent of the most rapid reconnection is $\Delta\psi = 1.1 \times 10^{21}$ Mx.

boundaries between the field lines rooted in these distinct regions become the separatrices, and their intersections are the separators. Once this distinction is made, topological reconnection (separator reconnection) is the only means of changing the amount of flux with a particular topology (Greene 1988; Lau & Finn 1990). Since field lines with an interconnecting topology cannot be produced through emergence they must result from separator reconnection.

The time history of the 171 Å loops suggests a highly intermittent reconnection process. Most of the reconnection occurs in a 3–6 hour interval whose onset is delayed by approximately 24 hours following the onset of flux emergence. We find nothing in the photospheric flux evolution at that time which could be construed as a trigger for this event. We are left to conclude that the reconnection episode is somehow triggered from the corona after roughly 24 hours of relatively quiet evolution. Some reconnection does occur during the quiet build-up phase, since at least 8 different interconnecting loops are visible, the first with incontrovertible connection appearing only 7 hours after the onset of emergence. But the reconnection rate during this period is evidently very low.

All interconnecting loops we observe are relatively narrow, as is typical of TRACE EUV observations. A loop of median diameter, $d = 3.7$ Mm (still well above the resolution limit), corresponds to a bundle of $\sim 4 \times 10^{18}$ Mx of magnetic flux. One explanation for this structuring is a reconnection process which is also spatially intermittent, or patchy, and reconnects discrete bundles of flux of approximately this size. Prior evidence for patchy reconnection has been found in down-flowing plasma voids following eruptive flares (McKenzie 2000) and in flux transfer events in the Earth's magnetosphere (Russell & Elphic 1978). If it is also responsible for setting the size of interconnecting loops then the present observation provides the first estimate of its scale at least in non-flaring reconnection.

5.1. *Potential inaccuracies in the flux estimates*

We have used the coronal loops, observed at 171 Å, to estimate the total flux transferred into the interconnecting domain. There are several uncertainties in this process which prevent us from obtaining a firm value. The most significant uncertainty stems from our inability to measure the magnetic field strength B_0 within the coronal loops. A potential field extrapolated from point sources has a separator with an apex field strength of 30 Gauss. Since interconnecting loops must lie below the separator, and the field is probably not potential, 30 G can be taken as a lower bound on the actual field strength. A field line underneath the separator, whose shape resembles one of the EUV loops (Loop 4) has a field strength 37 G at the point it crosses the slit (33 Mm). The field strength increases downward, and is $B_0 \simeq 70$ G at a height of 20 Mm. The presence of current in the field could also increase the field strength: in linear force-free fields with $|\alpha| \leq 0.02\,\mathrm{M}^{-1}$ the field strength at the 33 Mm point is as large as $B_0 \simeq 70$ G. We therefore conclude that the actual field strength within each loop is at least 37 G, but is probably larger but as much as a factor of 2.

The observed coronal loops bear a striking resemblance to the field lines in our potential field extrapolation (see fig. 12) suggesting that the potential approximation is a reasonable one, at least on the active-region scale. In light of this we feel it is unlikely that the true value of B_0 could exceed a value of 37 G by very much. Thus the 43 observed loops appear to account for 2–6$\times 10^{20}$ Mx of interconnecting flux. In further discussion we adopt an intermediate value, $\Delta\psi_{171} = 4 \times 10^{20}$ Mx, as the reconnected flux observed in TRACE 171Å.

In order for the magnetic field to remain potential, or even approximately potential, it would need to transfer $\Delta\psi \simeq 1.5 \times 10^{21}$ Mx: four times what we observe. It is theoretically possible that the reconnection is incomplete, and the field never fully relaxes. If the interconnecting domain were deprived of 75% of its flux, however, it would be smaller than the potential field, whose separatrices are plotted on stack plot fig. 2, by a factor even smaller than one-fourth (that is 1/4 of the cross-section, meaning 1/2 of the apparent width). During the period of intensive reconnection, however, loops are observed over the entire width spanned by the potential separatrices. This suggests that the interconnecting domain is almost as wide as in the potential field, and must therefore contain almost as much magnetic flux.

Where, then, is the rest of the interconnecting flux? There are several ways in which we might have undercounted the flux; even in those loops we did observe. For instance, one continuous streak on the stack plot, which we designate as a single loop, might actually consist of multiple sequential brightenings at closely spaced locations. This possibility, a spiritual relative of the "nanoflare hypothesis", was neglected under assumption number 3, that each loop tracks a single bundle of flux. An alternative conjecture that each loop was actually three or four different loops brightening in rapid succession, would account for the flux discrepancy and also bring the individual durations into agreement with their radiative lifetimes (see fig. 15). Such a model has been found to fit the observed behavior of active region loops observed in TRACE (Warren et al. 2003). In the present observation, however, this hypothesis raises a host of new questions. How do four neighboring flux bundles, all created by reconnection 3–6 hour earlier, suddenly brighten with such well-time synchronization that they cannot be distinguished from one another?

A more straightforward possibility is that TRACE 171 Å observations simply miss much of the flux. One possibility is that 75% of the flux is in loops so narrow ($d < 0.7$ Mm) or containing so little emission measure that they have evaded detection. Unresolved loops within the TRACE temperature band would presumably contribute to a diffuse background of emission. We have subtracted from the TRACE data the mean background level from the quiet Sun corona (Cirtain 2005). It is possible that reconnection had such a negligible effect on most of the flux that its intensity remained at or barely above this background level. Figure 7 shows that the majority of emission above the quiet Sun background level has been attributed to identified loops, especially during the reconnection episode. This seems to leave little room for the remaining 75% of the flux to have been significantly heated from reconnection.

The final possibility is that 75% of the flux in the interconnecting domain never cools to temperatures observable in Fe XI/X emission. This means, in effect, that the 171 Å has a gross filling factor of 25%. This is a reasonable possibility, since many coronal loop equilibrium models suggest that plasma above 2 MK should be relatively common, especially in long loops. It is not clear, however, that we can expect other coronal regions such as active region field, to have the same gross filling factor.

5.2. *The missing connection*

The absence of a second flux system from the purported reconnection poses a more puzzling instance of missing flux. Due to the nature of magnetic field lines, the act of reconnection should produce two distinct types of field lines. In the present scenario, reconnection will destroy field lines from domains $P051$–$N06$ and $P057$–$N01$ to create field lines in $P051$–$N01$ and $P057$–$N06$. This reconnection would be only the final one in a two-stage sequence required to create field lines interconnecting the two regions. Figure 10 shows that the $P051$–$N06$ field lines were themselves the product of reconnection along a $B1$–$A3$ separator which destroyed $P051$–$N30$ flux (in AR9574) and $P057$–$N06$ flux (in 9570). Since $N06$ is so very small this reconnection must be followed almost immediately by the one we have focused on, which creates $P051$–$N01$. We have observed field lines from this domain, but not from the second recipient domain: $P057$–$N06$. Where are the field lines of this domain?

The most obvious explanation is that flux in the second domain, $P057$–$N06$, is even harder to detect than that of the domain $P051$–$N01$ from which we may have missed 75%. Since the first post-reconnection domain lies under the separator, the second will lie above it. A typical field line from the potential model of domain $P057$–$N06$ at 6:30 Aug-11 is 270 Mm: more than twice as long as those typical of $P051$–$N01$. In equilibrium these long field lines will be half as dense and thus have one quarter the emission measure density, n_e^2, of their low-lying counterparts. This typical field line extends to a height of 84 Mm where its field strength of is 10 G, one quarter the value of the $P051$–$N01$ line. The pair of post-reconnection flux tubes will have equal flux giving the upper one twice the diameter. Combining their lower density and larger diameter the field lines from domain $P057$–$N06$ will be one-eighth as bright as those of $P051$–$N01$. We therefore propose that they would be too faint to be detectable in the present data.

5.3. *Energetics*

Our data are excellent for tallying reconnected flux, but are not ideally suited to quantifying the detailed energetics of the reconnection. We are, however, able to put some constraints on the energy liberation. The interconnecting loops cool gradually after reconnection, suggesting that a significant portion of the energy released is *not* directly converted to heat by the reconnection process. Had the reconnection converted magnetic energy into heat directly the loops would have cooled freely immediately after entering the interconnecting domain. This is contradicted by the much slower cooling implied by the 3-hour time delay between SXT and TRACE 171Å temperatures and the extended durations of all loops within the 171Å pass band.

The slow cooling suggests a continued heating following reconnection, at a gradually diminishing rate.

Following the logic above, the energy liberated by reconnection must have been dissipated (converted to heat) only gradually. All energy which is dissipated must, nevertheless, have been stored as magnetic energy prior to reconnection. The net stored energy must therefore match or exceed the total power dissipated over the extended dissipation period. We used two independent methods to place a lower bound on this integrated power.

The disk-integrated GOES X-ray observations can be used to derive the temperature (6–8 MK) and emission measure ($2 \times 10^{48}\,\mathrm{cm}^{-2}$) during the reconnection episode. The total power radiated by this plasma, over all wavelengths, during its appearance in GOES X-rays, is estimated to be 2.4×10^{30} ergs. This may include emission from outside the post-reconnection flux or from the $P057$–$N06$ domain. Indeed, the SXT images reveals the emerging AR (9574) to have 6 MK plasma amounting to one-half or one-third the emission measure of that seen in domain $P051$–$N01$.

An independent estimate comes from the loops observed in 171 Å. The average intensity of each loop was used to provide a lower bound on the electron density, n_e, by assuming that the plasma was at the optimal temperature for Fe XI/X emission. This lower bound was then used in an estimate of the total power density, $\mathcal{P}_r$, radiated over all wavelengths, which is therefore also an underestimate. Integrating the power radiated after one cooling time, and summing all loops observed between 9:00 and 12:00, yields 3.5×10^{28} ergs. Unlike the GOES X-ray measurement, this value includes only energy dissipated within the post-reconnection domain $P051$–$N01$. The value does, however, exclude a majority of the stored energy, even discounting the possibly higher electron densities. The observed loops had radiated most of their energy during the $\sim$ 3 hours prior to their cooling into the TRACE pass-band, and the loop-based estimate does not include this energy. It appears that a majority of the reconnected flux never cools into the TRACE pass-band, so its radiated energy is omitted altogether.

6. SUMMARY

6.1. *Observations*

The principle coronal observations presented here are high time-cadence 171 Å images of the regions between an emerging active region (9574) and an existing region (9570). We identify 43 instances of loops interconnecting these regions in a stack plot. There is at least one loop interconnecting the regions during most of the observation, but most of the loops occur during a three hour period. By attributing a single magnetic field strength B_0 to these loops and assuming that each interconnection is evident in 171 Å we calculated an electromotive force (EMF) from the reconnection between the regions. This curve is small until the 3-hour period of numerous interconnecting loops. Estimates of the plasma density within these loops, along with observations in soft X-rays (GOES and *Yohkoh*) indicate that the interconnecting loops are being heated over most of their lives.

A magnetic model of the two active regions is constructed from full disk MDI magnetograms. These were used to model the evolution of 36 distinct regions of concentrated flux. The four concentrations composing the emerging region increased and separated beginning at approximately 7:30 on Aug-10. The topology of the coronal field was modeled as a potential field anchored in point sources representing each of the concentrations. This model field included a domain of flux interconnecting one concentration (P051) from the emerging region to one (N01) in the pre-existing region. The flux in this model domain increases steadily, in contrast to the EMF inferred from the loop observations. The potential field extrapolation provides a value of the interconnecting field strength $B_0 \sim 37$ G, at positions just beneath the magnetic separator. Multiplying the EUV loops by this value results in an interconnecting flux smaller than the model's interconnecting domain by a factor of four.

6.2. *Interpretation*

To further summarize these observations we describe the model with which we have succeeded in interpreting the data. This model is offered as a method of organizing the observations and is probably not the only one consistent with the data.

Active region 9574 began emerging at 7:30 Aug-10 as its 10^{22} Mx flux tube crossed the photosphere, in the neighborhood of existing active region 9570. During the first 24 hours of emergence reconnection between the active regions proceeded slowly. The lack of reconnection caused magnetic stress to accumulate as current concentrated along the magnetic separator (see fig. 19). At around 6:00 Aug-11, when the accumulated current had reached $I \simeq 1.2 \times 10^{11}$ Amps, a brief reconnection episode was triggered. The reconnection persisted for 3 hours at an average loop-voltage of 10^9 Volts, leading to the transfer of $\simeq 10^{21}$ Mx across the separator. Localized patches of the separator current underwent reconnection to create flux bundles of $\sim 4 \times 10^{18}$ Mx each. The stressed field had accumulated at least $\Delta W \simeq 1.4 \times 10^{31}$ ergs, which was then released by the reconnection, but very little was dissipated directly at the separator. The released energy was converted instead into small-scale fluctuations such as a turbulence of Alfvén waves or tangled equilibrium field, whose energy was dissipated over the following 6 hours, causing the loops to cool and fade gradually.

This work was supported by NASA grant NAG5-10489. Portions of the work were completed at the Isaac Newton Institute at Cambridge University, where the manuscript benefited from useful comments offered by Klaus Galsgaard, Hugh Hudson, Clare Parnell and Lidia van Driel-Gesztelyi.

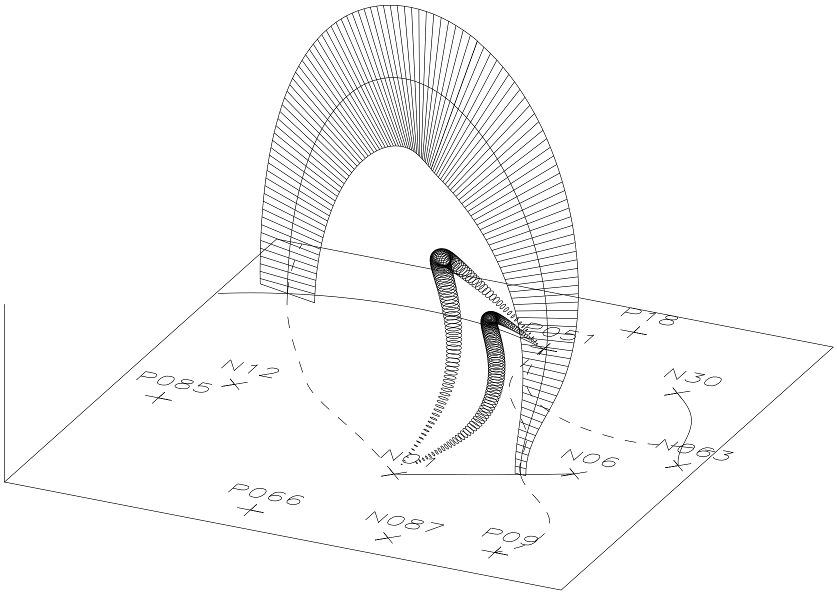

Fig. 19.— An illustration in perspective of the model of the reconnection between AR9570 and 9574. The vertical separator current sheet is shown as a skeleton, and a pair of reconnected flux tubes, 4×10^{18} Mx each, created by patches of reconnection on the separator current sheet, lie underneath it.

REFERENCES

Antiochos, S. K. 1998, ApJ, 502, L181

Aschwanden, M. J., Nightingale, R. W., & Alexander, D. 2000, ApJ, 541, 1059

Aschwanden, M. J., Schrijver, C. J., Winebarger, A. R., & Warren, H. P. 2003, ApJ, 588, L49

Berger, T. E., de Pontieu, B., Schrijver, C. J., & Title, A. M. 1999, ApJ, 519, L97

Berger, T. E., & Lites, B. W. 2003, Solar Phys., 213, 213

Bungey, T. N., Titov, V. S., & Priest, E. R. 1996, A&A, 308, 233

Cirtain, J. W. 2005, Ph.D. thesis, Montana State University

Fisher, G. H., Fan, Y., Longcope, D. W., Linton, M. G., & Pevtsov, A. 2000, Solar Phys., 192, 119

Fletcher, L., & Hudson, H. 2001, Solar Phys., 204, 69

Freeland, S. L., & Handy, B. N. 1998, Solar Phys., 182, 497

Garcia, H. A. 1994, Solar Phys., 154, 275

Golub, L., Krieger, A. S., Harvey, J. W., & Vaiana, G. S. 1977, Solar Phys., 53, 111

Greene, J. M. 1988, JGR, 93, 8583

Handy, B. N., et al. 1999, Solar Phys., 187, 229

Lau, Y.-T., & Finn, J. M. 1990, ApJ, 350, 672

Longcope, D. W. 1996, Solar Phys., 169, 91

Longcope, D. W. 2001, Phys. Plasmas, 8, 5277

Longcope, D. W., & Cowley, S. C. 1996, Phys. Plasmas, 3, 2885

Longcope, D. W., & Klapper, I. 2002, ApJ, 579, 468

Longcope, D. W., & Magara, T. 2004, ApJ, 608, 1106

Longcope, D. W., & Silva, A. V. R. 1998, Solar Phys., 179, 349

McKenzie, D. E. 2000, Solar Phys., 195, 381

McKenzie, D. E. 2002, in Multi-Wavelength Observations of Coronal Structure and Dynamics – Yohkoh 10th Anniversary Meeting, ed. P. C. H. Martens & D. Cauffman, COSPAR Colloquia Series (Elsevier), 155

Parker, E. N. 1972, ApJ, 174, 499

Pevtsov, A. A. 2000, ApJ, 531, 553

Priest, E. R., & Démoulin, P. 1995, JGR, 100, 23,443

Rosner, R., Tucker, W. H., & Vaiana, G. S. 1978, ApJ, 220, 643

Russell, C. T., & Elphic, R. C. 1978, Space Sci. Rev., 22, 681

Scherrer, P. H., et al. 1995, Solar Phys., 162, 129

Sheeley, N. R., Bohlin, J. D., Brueckner, G. E., Purcell, J. D., Scherrer, V., & Tousey, R. 1975, Solar Phys., 40, 103

Sweet, P. A. 1958, Nuovo Cimento, 8, 188

Thomas, R. J., Crannell, C. J., & Starr, R. 1985, Solar Phys., 95, 323

Titov, V. S., Hornig, G., & Démoulin, P. 2002, JGR, 107, 3

Tsuneta, S. 1996, ApJ, 456, L63

Tsuneta, S., et al. 1991, Solar Phys., 136, 37

Warren, H. P., Winebarger, A. R., & Mariska, J. T. 2003, ApJ, 593, 1174